

Semiconductor heterostructures and device structures investigated by photoreflectance spectroscopy

JAN MISIEWICZ^{*}, PIOTR SITAREK, GRZEGORZ SĘK, ROBERT KUDRAWIEC

Institute of Physics, Wrocław University of Technology,
Wybrzeże Wyspiańskiego 27, 50-370 Wrocław, Poland

In this review, we present the photoreflectance (PR) spectroscopy as a powerful tool for investigations of bulk semiconductors and semiconductor heterostructures. We discuss the application of PR technique to investigation of various properties of semiconductors, including the composition of ternary compounds, distribution of the built-in electric field and the influence of perturbations such as temperature, strain, pressure; low-dimensional structures such as quantum wells, multiple quantum wells and superlattices, quantum dots; and the structures of semiconductor devices like transistors and vertical/planar light emitting laser structures.

Key words: photoreflectance; electric field; low-dimensional structures; semiconductor devices

1. Introduction

Because of their novel physical properties and device applications, new materials and based on them semiconductor heterostructures such as quantum wells (multiple quantum wells, superlattices) and heterojunctions have been produced. To explore various physical properties of these materials and structures based on them, a number of characterisation methods, including photoluminescence (PL)^{**}, photoluminescence excitation (PLE) spectroscopy, transmission electron microscopy (TEM), X-ray techniques, Hall measurements, etc., have been applied. Most of the above-mentioned methods require special experimental conditions such as low temperatures (PL, PLE), or special sample preparation (TEM, Hall measurements). For practical applications, it is advantageous to use techniques, which are simple and at the same time provide a lot of valuable information. Such are electro-modulation spectroscopy techniques.

^{*}Corresponding author, e-mail: Jan.Misiewicz@pwr.wroc.pl.

^{**}See list of abbreviations, p. 301.

These methods were introduced in the sixties and were used in investigations of semiconductor band structure parameters in the seventies. We focus our attention on one particular contactless form of electric field modulation spectroscopy called photoreflectance (PR). Glembocki et al. in 1985 [1] reported the first application of photoreflectance to studies of semiconductor microstructures. Because of its extreme sensitivity to interband electronic transitions, many papers on this subject have been published since 1985. A number of review papers about the application of photoreflectance spectroscopy to the investigation of semiconductors and semiconductor structures have been published up to now [2–8].

In this paper, we present applications of the photoreflectance spectroscopy for investigations of bulk semiconductors, epilayers and low-dimensional semiconductor structures which provide studying and understanding the optical processes in semiconductor device structures. We start with a brief theoretical background to the technique and lineshape formulas associated with photoreflectance.

2. Principles of photoreflectance spectroscopy

Since its inception in the sixties, modulation spectroscopy has proven to be a powerful experimental technique for studying and characterization bulk semiconductors, reduced dimensional systems (surfaces, interfaces, quantum wells, wires and dots, etc.), actual device structures (transistors, lasers) and growth/processing. A derivative of an optical spectrum (i.e. of the reflectivity) with respect to some parameter is evaluated with any modulation spectroscopy. The measured optical signal depends on the joined density of states making this method sensitive to transitions at the critical point in the Brillouin zone of the material studied. The resulting spectrum has sharp, derivative-like features on a featureless background. Figure 1 shows the comparison of the reflectivity and electroreflectance spectra for bulk GaAs at 300 K [5, 9, 10]. While the reflectivity is characterized by broad features, the electroreflectance (ER) modulation spectrum is dominated by a series of very sharp lines with a zero signal as a baseline.

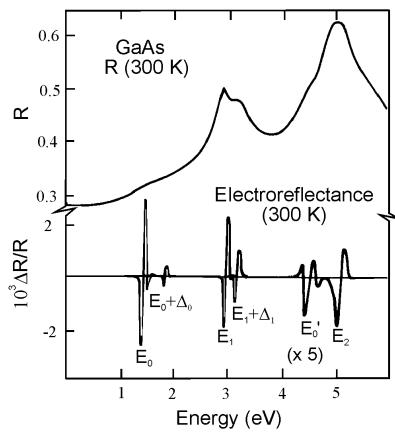


Fig. 1. Comparison of room-temperature reflectivity and electroreflectance of GaAs [5, 9, 10]

The modulation can easily be accomplished by varying some parameters, associated with the sample or the experimental system, in a periodic fashion and measuring the corresponding normalised change of the optical properties. It is possible to modulate a variety of parameters, i.e. the wavelength of light, temperature, stress applied or electric field in the sample studied. The electromodulation techniques are based on the modulation of the electric field. One of the electromodulation techniques is photoreflectance spectroscopy where the varying parameter is the internal (built in the structure) electric field.

In the PR, the modulation of the electric field in the sample is caused by photo-excited electron-hole pairs created by the pump source (usually laser) which is chopped with a given frequency. The photon energy of the pump source is generally above the band gap of the semiconductor being under study. There is a possibility to use a below band-gap modulation through the excitation of impurity or surface states [11]. The mechanism of the photo-induced modulation of the built-in electric field F_{DC} is explained in Fig. 2, for the case of an n-type semiconductor. Because of the pinning of the Fermi energy E_F at the surface, there exists a space-charge layer. The occupied surface states contain electrons from the bulk (Fig. 2a). Photoexcited electron-hole pairs are separated by the built-in electric field, with the minority carrier (holes in this case) being swept toward the surface. At the surface, the holes neutralize the trapped charge, reducing the built-in field from F_{DC} to $F_{DC}-F_{AC}$, where F_{AC} is a change in the built-in electric field (Fig. 2b).

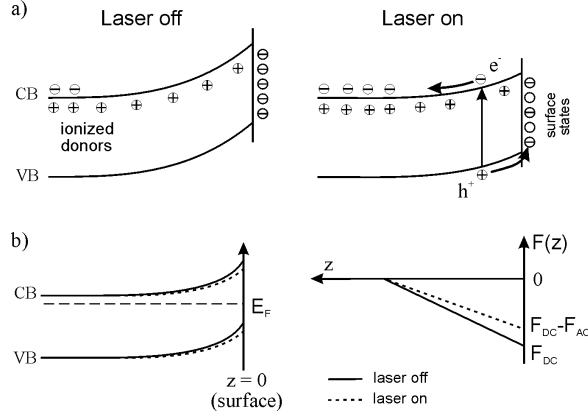


Fig. 2. Schematic representation of the photoreflectance effect (a), and the photoinduced changes in electronic bands and the surface built-in electric field (b), for an n-type semiconductor

In photoreflectance spectroscopy, relative changes in the reflectivity coefficient are measured. The changes we can define as

$$\frac{\Delta R}{R} = \frac{R_{\text{off}} - R_{\text{on}}}{R_{\text{off}}} \quad (1)$$

In the above expression R_{off} and R_{on} are the reflectivity coefficients, when the pump beam (laser) is off and on, respectively. These normalized changes can be related to the perturbation of the dielectric function ($\varepsilon = \varepsilon_1 + i\varepsilon_2$) expressed as [12]

$$\frac{\Delta R}{R} = \alpha(\varepsilon_1, \varepsilon_2)\Delta\varepsilon_1 + \beta(\varepsilon_1, \varepsilon_2)\Delta\varepsilon_2 \quad (2)$$

where α and β are the Seraphin coefficients, related to the dielectric function, and $\Delta\varepsilon_1$ and $\Delta\varepsilon_2$ are related by Kramers–Kronig relations.

We will discuss the lineshapes of the PR response in terms of electromodulation mechanisms. Electromodulation can be classified into three categories depending on the relative strengths of characteristic energies [13]. In the low-field regime $|\hbar\Omega| \leq \Gamma$, where $\hbar\Omega$ is the electro-optic energy given by:

$$(\hbar\Omega)^3 = \frac{q^2 \hbar^2 F^2}{2\mu} \quad (3)$$

In the above equation, F is the electric field, μ is the reduced interband mass in the direction of the field. In the intermediate-field case, when $|\hbar\Omega| \geq \Gamma$ and $qFa_0 \ll E_g$ (a_0 is the lattice constant), the Franz–Keldysh oscillations (FKO) appear in the spectrum. In

the high-field regime the electro-optic energy is much greater than the broadening but $qFa_0 \approx E_g$ so that the Stark shifts are produced.

Recently, Pollak [5] as well as Glembocki and B.V. Shanabrook [2] provided a most detailed theoretical background of the photoreflectance technique.

2.1. Low field limit – third-derivative spectroscopy

Due to the modulation of the electric field, the perturbation destroys the translational symmetry of the crystal and hence can accelerate free charge carriers [14, 15]. In effect, under certain electric field conditions, the electromodulation results in sharp, third-derivative lineshapes.

For Lorentzian form of the dielectric function, low-field modulation, and under a parabolic band approximation, one can rewrite Eq. (2) as [13]

$$\frac{\Delta R}{R} = \text{Re} \left[A e^{i\varphi} (E - E_g + i\Gamma)^{-m} \right] \quad (4)$$

where E_g is a band gap energy, Γ is the broadening parameter ($\Gamma \sim \hbar/\tau$), A and φ are the amplitude and phase factor, respectively. The parameter m in the lineshape factor of Eq. (4) depends on the type of the critical point. In a three-dimensional system, m equals 2.5, while for a two-dimensional critical point $m = 3$.

2.2. Low field limit – first-derivative spectroscopy

The perturbation due to the changes of the electric field does not accelerate charge carriers in their bound states such as excitons, quantum wells or impurities. These types of particles are confined in space which does not have a translational symmetry. For bound states, the photoreflectance lineshape has a first-derivative character [16], and the changes in the dielectric function may be expressed as

$$\Delta \varepsilon = \left[\frac{\partial \varepsilon}{\partial E_g} \frac{\partial E_g}{\partial F_{AC}} + \frac{\partial \varepsilon}{\partial \Gamma} \frac{\partial \Gamma}{\partial F_{AC}} + \frac{\partial \varepsilon}{\partial I} \frac{\partial I}{\partial F_{AC}} \right] F_{AC} \quad (5)$$

where F_{AC} is the change in the built-in electric field and I is the intensity of the optical transition. Equation (5) can be rewritten as [17]

$$\Delta \varepsilon_i = \left[A_E f_E^i + A_\Gamma f_\Gamma^i + A_I f_I^i \right] \frac{I}{\Gamma} F_{AC}, \quad i = 1, 2 \quad (6)$$

with

$$\begin{aligned}
A_E &= \frac{1}{\Gamma} \frac{\partial E_g}{\partial F_{AC}}, & f_E^i &= \frac{\partial \varepsilon_i}{\partial E_g} \\
A_\Gamma &= \frac{1}{\Gamma} \frac{\partial \Gamma}{\partial F_{AC}}, & f_\Gamma^i &= \frac{\partial \varepsilon_i}{\partial \Gamma} \\
A_I &= \frac{1}{I} \frac{\partial I}{\partial F_{AC}}, & f_I^i &= \frac{\partial \varepsilon_i}{\partial I}
\end{aligned} \tag{7}$$

Depending on the broadening mechanism (i.e. temperature), the unperturbed dielectric function can be either Lorentzian or Gaussian. For quantum wells, the dielectric function is excitonic, even at elevated temperatures. Thus for the quantum microstructures, the Lorentzian or Gaussian profiles of dielectric function are appropriate. The Lorentzian dielectric function can be written as [15]

$$\varepsilon = 1 + \frac{I}{E - E_g + i\Gamma} \tag{8}$$

The modulation terms of Eq. (6) are given by

$$\begin{aligned}
f_E^1 &= \frac{y^2 - 1}{(y^2 + 1)^2}, & f_\Gamma^1 &= f_E^2, & f_I^1 &= \frac{y}{y^2 + 1} \\
f_E^2 &= \frac{-2y}{y^2 + 1}, & f_\Gamma^2 &= -f_E^1, & f_I^2 &= \frac{-1}{y^2 + 1}
\end{aligned} \tag{9}$$

where

$$y = \frac{E - E_g}{\Gamma} \tag{10}$$

If the intensity modulation terms are ignored, only two independent lineshape factors (see Eq. (9)) do not vanish. The combined spectral dependence can then be expressed by Eq. (4) with $m = 2$ [15].

The unperturbed dielectric function of a Gaussian profile is given by [17]

$$\varepsilon = 1 + I (L_1 + i L_2) \tag{11}$$

where

$$\begin{aligned}
L_1 &= \frac{y}{\Gamma} \Phi(1, 3/2, -y^2/2) \\
L_2 &= \sqrt{\frac{\pi}{2}} \frac{1}{\Gamma} \exp(-y^2/2)
\end{aligned} \tag{12}$$

Φ is the confluent hypergeometric function. In this case, the modulation terms of Eq. (6) can be written as

$$\begin{aligned}
 f_E^1 &= -\Phi(1, 1/2, -y^2/2) \\
 f_E^2 &= -\sqrt{\frac{\pi}{2}} y \exp(-y^2/2) \\
 f_I^1 &= -2y \Phi(2, 3/2, -y^2/2) \\
 f_I^2 &= -\sqrt{\frac{\pi}{2}} (y^2 - 1) \exp(-y^2/2) \\
 f_I^1 &= y \Phi(1, 3/2, -y^2/2) \\
 f_I^2 &= -\sqrt{\frac{\pi}{2}} \exp(-y^2/2)
 \end{aligned} \tag{13}$$

Hence, for the dielectric function of the Gaussian type one can get

$$\frac{\Delta R}{R} = [Af_E^1 + Bf_E^2] \tag{14}$$

2.3. Intermediate field limit – Franz–Keldysh oscillations

When the low-field criteria are not satisfied, but $eFa_0 \ll E_g$, the dielectric function can exhibit the Franz–Keldysh oscillations. Although the exact form of $\Delta R/R$ for the intermediate-field case with the broadening is quite complicated, Aspnes and Studna [10] derived a relatively simple expression

$$\frac{\Delta R}{R} \propto \frac{1}{E^2(E - E_g)} \exp \left[-2(E - E_g)^{1/2} \frac{\Gamma}{(\hbar\Theta)^{3/2}} \right] \cos \left[\frac{4}{3} \frac{(E - E_g)^{3/2}}{(\hbar\Theta)^{3/2}} + \chi \right] \tag{15}$$

From the above equation, the position of an n -th extreme in the Franz–Keldysh oscillations is given by

$$n\pi = \frac{4}{3} \left[\frac{E_n - E_g}{\hbar\Theta} \right]^{3/2} + \chi \tag{16}$$

where E_n is the photon energy of the n -th extreme and χ is an arbitrary phase factor [18]. A plot $[4/(3\pi)](E_n - E_g)^{3/2}$ vs. the index number n will yield a straight line with the slope $(\hbar\Theta)^{3/2}$. Therefore, the electric field F can directly be obtained from the period of FKO if μ is known. Conversely, μ can be measured if the electric field is known.

The dominant field in the structure determines the period of the FKO. In the above expressions the nature of that field was not specified. There are two limiting cases to be considered. If modulation is from a flat band, i.e. no presence of a DC field, then the field is clearly the modulating field F_{AC} . A more interesting situation occurs when there exists a large DC electric field in the material and a small modulating field is applied, i.e. $F_{AC} \ll F_{DC}$. In this case, the period of the FKO is given by F_{DC} and not by F_{AC} [19]. Shen and Pollak [19] even considered the case when F_{AC} is not small compared to F_{DC} . They have shown that even for F_{AC}/F_{DC} as large as 0.15 the first few FKO are still determined by F_{DC} .

3. Experimental details

In Figure 3, a schematic diagram of the photoreflectance apparatus is shown. The probe light is a monochromatic beam obtained from a quartz halogen lamp dispersed through a monochromator. This beam of intensity I_0 is focused on the sample. The laser (pumping) beam illuminates the same spot of the sample. The laser beam is chopped with the frequency of a few hundreds Hz. The photon energy of the pump source should be generally above the band gap of the semiconductor being investigated. A He-Ne laser (the energy range below 1.96 eV) or Ar⁺ ion laser (the energy range below 4.5 eV) are used as typical pump sources. The intensity of the laser light can be adjusted by a variable, neutral density filter. The light reflected from the sample is detected by a photodiode or a photomultiplier. In order to prevent the detection of laser light, an appropriate longpass glass filter is used in front of the photodetector. The signal separator, connected to the detector, separates the signal into two components. The DC component is proportional to I_0R , and AC component is proportional to $I_0\Delta R$. The AC component is measured with a lock-in amplifier. A computer divides the AC signal by the DC component giving the photoreflectance spectrum, $\frac{\Delta R}{R}(\omega)$, where $\hbar\omega$ is the photon energy of the incident beam.

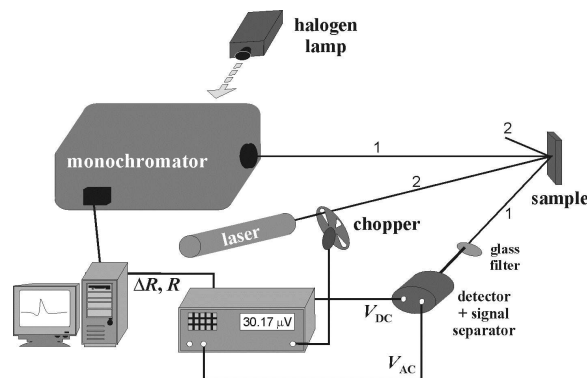


Fig. 3. Schematic diagram of the photoreflectance apparatus

In the case of photoreflectance, efficient filtering of the stray laser light is required, because it has the same frequency (chopped) as the signal of interest and can easily be detected. The scattered pump light can be reduced by means of an appropriate longpass filter in front of the detector. Furthermore, the laser illumination can produce a band-gap photoluminescence, which under certain conditions is more intense than the signal of interest. This problem can be eliminated by using long-focal-length optics or by using a second monochromator running in unison with the probe monochromator [20]. For a double monochromator, two scans are taken: one with the probe light on and one without it. Subtracting the two traces effectively eliminates the PL. An alternative technique involves using a dye laser as the probe beam and a detector placed sufficiently far away from the sample so as to reduce the PL, which is usually emitted isotropically [16, 21]. The spurious photoluminescence background signal can also be reduced or eliminated by approaches such as the use of double detector system [22], sweeping photoreflectance [23], or double pump beam method called differential photoreflectance [24].

4. Properties of semiconductor bulk and epilayers

A study of separated layers (or thin films) and its properties is a preliminary work to the investigation of more complicated structures (e.g. quantum wells, etc.) and, finally, semiconductor device structures. Here we will discuss the use of the photoreflectance spectroscopy to study bulk properties of semiconductors such as the composition of multinary semiconducting compounds, carrier concentration, distribution of the built-in electric field, the influence of perturbations like temperature and strain. Although a number of investigations have actually been performed on epitaxial (or thin) layers, the results do not explicitly depend on the nature of the films but they are the consequence of bulk properties.

4.1. Composition of alloys

One of the extremely important parameters of a semiconductor is the composition of binary A_xB_{1-x} , ternary $A_xB_{1-x}C$ or quaternary $A_xB_{1-x}C_yD_{1-y}$ alloys. The compositional variation of the fundamental transition (E_0) and/or features lying at higher energies (E_1) have been investigated by photoreflectance for a large number of alloys including, $Cd_{1-x}Mn_xTe$ (for $x \leq 0.6$) at room and liquid helium temperatures [25], $Al_xIn_{1-x}P$ [26], $CuAl_xGa_{1-x}Se_2$ [27], $CuAl(S_xSe_{1-x})_2$ [28], ZnO on $ScAlMgO_4$ [29], $In_xGa_{1-x}N$ [30] and $Al_xGa_{1-x}As$, for $x \leq 0.6$ [31, 32].

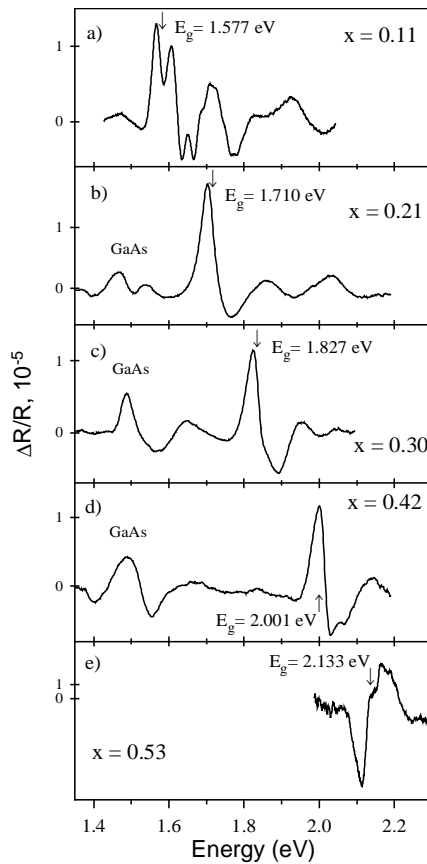


Fig. 4. Room-temperature PR spectra of $\text{Al}_x\text{Ga}_{1-x}\text{As}/\text{GaAs}$ structures as a function of aluminium content x . Arrows mark the band gap energies of $\text{Al}_x\text{Ga}_{1-x}\text{As}$ (after Sitarek et al. [32])

In Figure 4, the PR spectra obtained by Sitarek et al. [32] of several $\text{Al}_x\text{Ga}_{1-x}\text{As}$ layers grown by MBE (molecular beam epitaxy) on GaAs substrates are shown vs. the aluminium content. The spectra are quite complicated because the Franz–Keldysh oscillations are present and also the signal related to the GaAs buffer is seen. Using the transition energies derived from the spectra, the dependence of the E_0^{AlGaAs} on the composition has been determined as

$$E_0(x) = (1.430 \pm 0.004) + (1.34 \pm 0.02)x \quad (17)$$

Equation (17) was compared with the literature data [33]. The comparison is presented in Fig. 5.

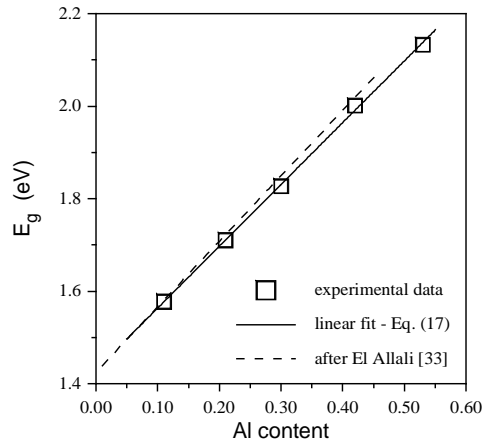


Fig. 5. The band gap energy of $\text{Al}_x\text{Ga}_{1-x}\text{As}/\text{GaAs}$ vs. aluminium content from PR experiment (squares) (see Fig. 4). Solid line – linear approximation to the experimental data; dashed line – taken after [33] (after Sitarek et al. [32])

4.2. Carrier concentration

There are few reports on the application of the photoreflectance spectroscopy to the investigation of carrier concentration and relation between dopants concentration and free carrier concentration. Peters et al. [34] used the photoreflectance spectroscopy as a method for calibration of the n-type doping in Si-doped GaAs. Having studied the blue shift of the fundamental band gap of GaAs with the increasing doping concentration, they found a linear correlation between the dopant concentration and the value of the shift of the energy gap. They explained this effect as the result of the competition between the many-body effects and the Burstein–Moss effect related to the filling of the conduction band. Such an effect has also been observed in the n-type [35] and p-type [36] GaAs. Lee et al. [35] extended the results of Peters et al. [34] for Si-doped samples of concentrations from $1 \times 10^{17} \text{ cm}^{-3}$ up to almost $1 \times 10^{19} \text{ cm}^{-3}$.

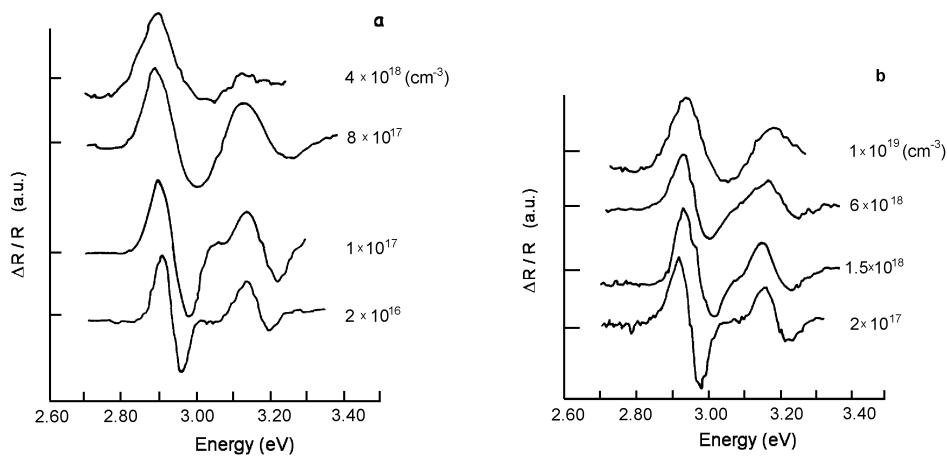


Fig. 6. PR response of GaAs as a function of carrier concentration: a) for GaAs:Si; b) for GaAs:Zn (after Badakhshan et al. [38])

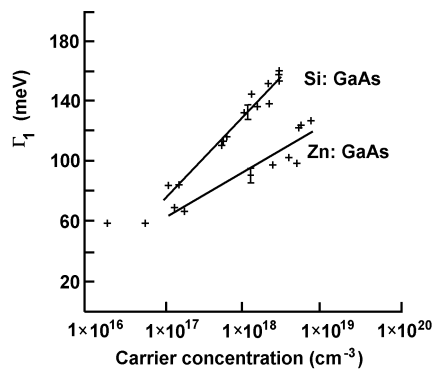


Fig. 7. The PR broadening parameter as a function of carrier concentration (after Badakhshan et al. [38])

Similar effects were investigated using PR for Si-doped GaN layers grown by the metal-organic chemical vapour deposition (MOCVD). In this case, a linear dependence between the fundamental gap transition energy and the cubic root of the carrier concentration has been found [37]. This red shift of the band gap with the increase of the level of Si doping has been fully explained by the many-body effects (the renormalisation of the band gap).

The effects of the carrier concentration manifest themselves not only at the fundamental band gap. Badakhshan et al. [38] investigated the PR spectra of MOCVD-grown GaAs:Si (n-type) and GaAs:Zn (p-type) layers in the range of E_1 and $E_1+\Delta$ transitions. They observed almost no shift in their energy but a very strong increase of the broadening parameter Γ_1 with the increase of the carrier concentration. In Fig. 6, the PR spectra as a function of doping concentration and doping type are shown. In Fig. 7, the linear dependence of broadening vs. logarithm of the carrier concentration is presented.

4.3. Temperature dependence

The temperature dependence of the energy and broadening parameter of the band gap of a semiconductor can be the source of different information about the scattering effects. The two most popular relations describing the temperature dependence of band gap are: the semiempirical Varshni expression [39]

$$E_0(T) = E_0(0) - \frac{\alpha T^2}{\beta + T} \quad (18)$$

and the Bose–Einstein expression [40, 41]

$$E_0(T) = E_0(0) - \frac{2a_B}{\exp(\Theta_B/T) - 1} \quad (19)$$

where a_B represents the strength of the electron–average phonon interaction and Θ_B corresponds to an average phonon temperature. The temperature shift $E_0(T)$ contains contributions from both thermal expansion and electron–phonon coupling effects.

The variation of the linewidth (broadening parameter) with temperature can be also expressed by the Bose–Einstein type expression [40, 41]

$$\Gamma(T) = \Gamma(0) + \frac{\Gamma_{LO}}{\exp(\Theta_{LO}/T) - 1} \quad (20)$$

The first term of this equation corresponds to the broadening mechanisms due to intrinsic lifetime, electron–electron interaction, impurity, dislocation and alloy scattering effects. The parameter Γ_{LO} is an electron–LO phonon coupling constant and Θ_{LO} is the LO phonon temperature.

The photoreflectance spectroscopy has been used to measure the temperature variation of the energy gap of GaAs [42, 43], InP [44], $\text{Al}_{0.18}\text{Ga}_{0.82}\text{As}$ [42, 45], $\text{In}_x\text{Ga}_{1-x}\text{As}$ on GaAs for various values of x [46–49], $\text{In}_{0.53}\text{Ga}_{0.47}\text{As}$ on InP (also for the $E_0+\Delta_0$ transition) [50], $\text{In}_{0.515}\text{Ga}_{0.485}\text{As}$ on InP [51,52], GaSb, $\text{In}_x\text{Ga}_{1-x}\text{As}_y\text{Sb}_{1-y}$ on GaSb [53], CdTe [54], $\text{Cd}_{0.72}\text{Mn}_{0.28}\text{Te}$ [55], $\text{Cd}_{0.9}\text{Mn}_{0.1}\text{Te}$ [25], InAs [56], wurtzite-type GaN [57].

The temperature dependence of the fundamental band gap and broadening parameter of GaSb and $\text{In}_x\text{Ga}_{1-x}\text{As}_y\text{Sb}_{1-y}$ alloys between 14 and 377 K were studied by Muñoz et al. [53]. The four quaternary samples have the compositions (x, y) : (0.07, 0.05), (0.09, 0.07), (0.12, 0.11), (0.22, 0.19). The values of $E_0(T)$ obtained from PR measurements for all samples being under study are shown by solid lines in Fig. 8. The quantity $E_0(T)$ was taken from the fit to the experimental data with the Varshni and Bose–Einstein expressions (Eqs. (18) and (19)). As a consequence of the above analysis, Muñoz et al. obtained the correct value (comparable with previous results) for $E_0(0)$ equal to 0.809 eV for GaSb and the corresponding ones for the quaternary compounds.

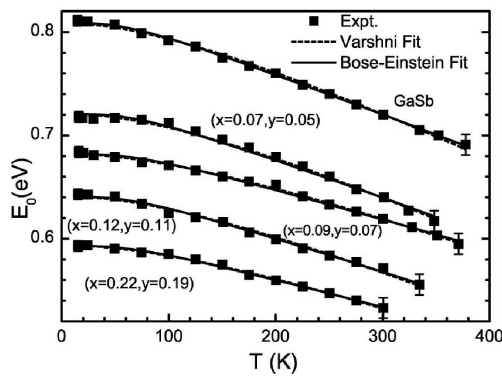


Fig. 8. Experimental values of $E_0(T)$ vs. T for different samples (solid squares); the (x, y) notation – the composition of the quaternary samples; the dashed and continuous lines – the fits according to the Varshni relation (Eq. (18)) and the Bose–Einstein (Eq. (19)) expression, respectively (after Muñoz et al. [53])

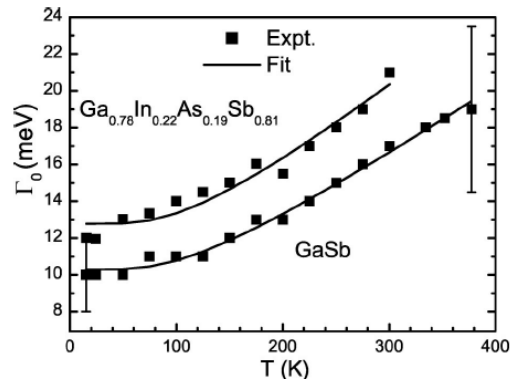


Fig. 9. $\Gamma_0(T)$ vs. T for the GaSb and $\text{In}_{0.22}\text{Ga}_{0.78}\text{As}_{0.19}\text{Sb}_{0.81}$ samples (solid squares); the solid lines are the fit according to the Bose–Einstein relation (Eq. (20)). Representative bars are shown (after Muñoz et al. [53])

In Figure 9, closed squares are the experimental values of $\Gamma_0(T)$ for the GaSb and $\text{In}_{0.22}\text{Ga}_{0.78}\text{As}_{0.19}\text{Sb}_{0.81}$ samples, respectively. Because of the error bars on the above data, it was necessary to fix the parameter Θ_{LO} in order to obtain two significant quantities $\Gamma_0(0)$ and Γ_{LO} by means of a least-squares fit using a the Bose–Einstein equation (Eq. (20)) – solid lines in Fig. 9.

4.4. Influence of strain

One of the main goals of strained-layer epitaxy is to create metastable thin films with properties different from those of the corresponding bulk materials. Typically, such films are pseudomorphic compound semiconductor structures grown from lattice-mismatch materials by molecular beam epitaxy (MBE) or by metal-organic chemical-vapour deposition (MOCVD). Such structures offer nearly complete flexibility in tailoring their electronic and optical properties and have proven to be highly successful in novel microelectronic and optoelectronic devices. This flexibility is enhanced by the possibility of pseudomorphic growth, where the lattice mismatch between the epilayer and substrate is accommodated by elastic strain. In fact, the in-plane biaxial strain, arising at the interface with the substrate, considerably affects the electronic structure and the optical response of the epilayer. It changes the band gaps, depending on the sign of the strain, reduces or removes the interband or intraband degeneracies (e.g., between the heavy and light hole valence bands at $\mathbf{k} = 0$), and also reduces coupling between neighbouring bands.

Concerning the E_0 optical transitions at $\mathbf{k} = 0$, the hydrostatic component of the strain shifts the energy gaps between the valence bands and the lowest lying conduction band. In addition, the uniaxial strain component splits the heavy (HH) and light (LH) hole valence bands. The resulting energy gaps between the conduction and the split valence bands are

$$E_0^{HH} = E_0 + \delta E_H - \frac{\delta E_S}{2} \quad (21)$$

$$E_0^{LH} = E_0 + \delta E_H + \frac{\delta E_S}{2} - \frac{(\delta E_S)^2}{2\Delta_0} \quad (22)$$

where

$$\delta E_H = 2a \frac{C_{11} - C_{12}}{C_{11}} \varepsilon \quad (23)$$

$$\delta E_S = 2b \frac{C_{11} + 2C_{12}}{C_{11}} \varepsilon \quad (24)$$

while C_{ij} are the elastic stiffness constants, a and b are the hydrostatic and shear deformation potentials, respectively and ε is the in-plane strain which is given by $\varepsilon = (a_S - a_L)/a_L$, where a_S and a_L are the lattice parameters of the substrate and layer, respectively. The valence band splitting, as measured from the optical spectra, is

$$\Delta E_{\text{split}} = \delta E_S = 2b \frac{C_{11} + 2C_{12}}{C_{11}} \varepsilon \quad (25)$$

The PR spectra showing the heavy- and light-hole splitting generated by strain in GaAs layers deposited on Si substrates [58] are visible in Fig. 10. The quantity ΔE stands for the splitting between light (feature A) and heavy (feature B) hole bands. The value of the splitting increases on lowering the temperature. It has been explained on the base of the difference in the thermal expansion coefficients of GaAs and Si. From the value of the splitting energy expressed by Eq. (25), the value of the in-plane strain was estimated to be 0.12% being in agreement with the X-ray diffraction results.

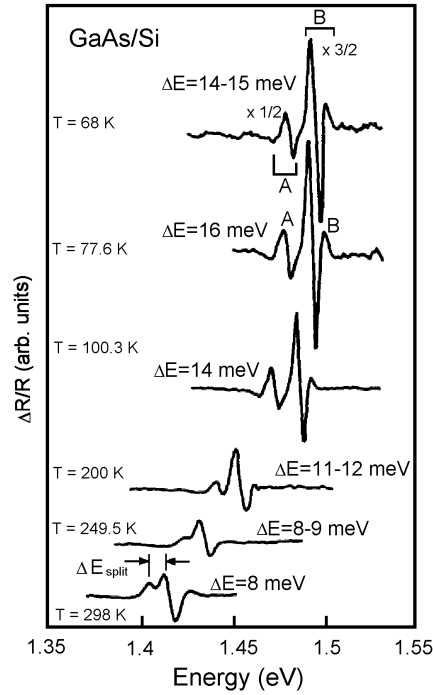


Fig. 10. PR spectra of strained GaAs on Si at several temperatures (after Glembocki [58]). A and B are the light and heavy hole transitions, respectively

The required strain-dependent properties can be achieved only by careful controlling the composition and the epilayer thickness, which should be lower than a critical value d_c to avoid relaxation via misfit dislocations which drastically degrade the layer quality and hence also the device performance. This problem has also been investigated by means of the photoreflectance spectroscopy for $\text{In}_x\text{Ga}_{1-x}\text{As}$ layers grown by MOCVD on GaAs substrates [59, 60]. S¸ek et al. determined the broadening parameter and the

PR amplitude of the band gap feature of the $\text{In}_x\text{Ga}_{1-x}\text{As}$ for several samples with various indium contents and epilayer thicknesses. An example of the spectrum is shown in Fig. 11. The dependences of the broadening parameter and PR amplitude vs. Δd are shown in Figs. 12 and 13. The quantity Δd is defined as the difference between the nominal layer thickness (determined from the growth conditions and X-ray diffraction measurements) and its critical value (taken from the theoretical dependence of the critical thickness vs. indium content of $\text{In}_x\text{Ga}_{1-x}\text{As}$ on GaAs [61]). A rapid increase of the broadening and decrease in the amplitude of the PR signal is observed at $\Delta d = 0$ due to the overcoming of the critical thickness and a strong degradation of the layer optical properties.

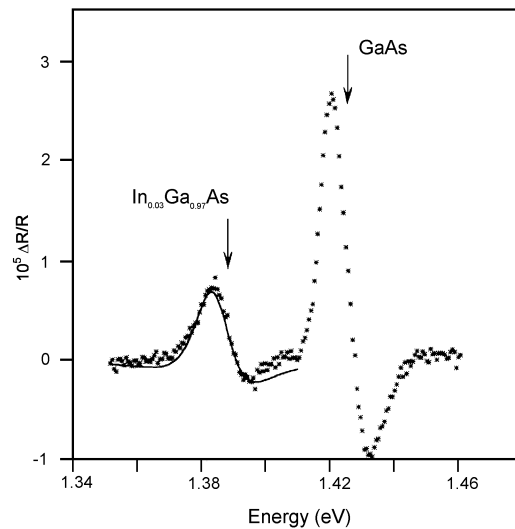


Fig. 11. Room-temperature PR spectrum of 100 nm thick strained $\text{In}_{0.03}\text{Ga}_{0.97}\text{As}$ layer on GaAs substrate (after Søk et al. [60])

Lastras-Martinez et al. [62] report on photoreflectance-difference (PRD) measurements of n-type (001) GaAs crystals under uniaxial stress along [110]. The authors study the difference between two photoreflectance spectra, one measured with unpolarized light and the other with linearly polarized light along one of the symmetry axis of the crystal. The PRD spectra were recorded in the 2.6–3.6 eV energy range around the E_1 and $E_1 + \Delta_1$ interband transitions of GaAs.

In general, PR spectra comprise, both linear electrooptic (LEO) and quadratic electro-optic (QEO) components, with this second component dominating the PR lineshape [62]. For light normally incident on the (001) surface of zinc blende crystal, nevertheless, the PRD spectrum comprises only a LEO component because the QEO term is isotropic for cubic symmetries. In addition to the previously reported LEO component [63], they have found a QEO component when stress is applied.

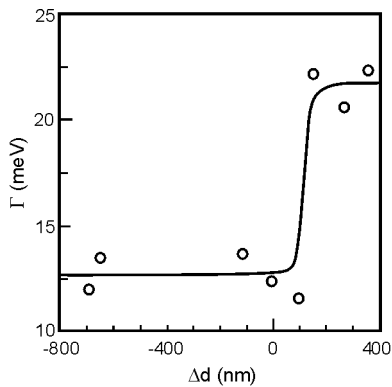


Fig. 12. The broadening parameter of the PR signal of several $\text{In}_x\text{Ga}_{1-x}\text{As}$ layers on GaAs vs. Δd (after Şek et al. [60])

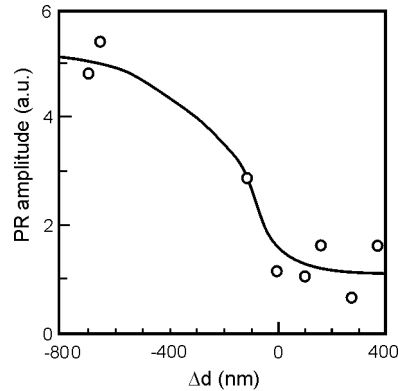


Fig. 13. The PR amplitude of several $\text{In}_x\text{Ga}_{1-x}\text{As}$ layers on GaAs vs. Δd (after Şek et al. [60])

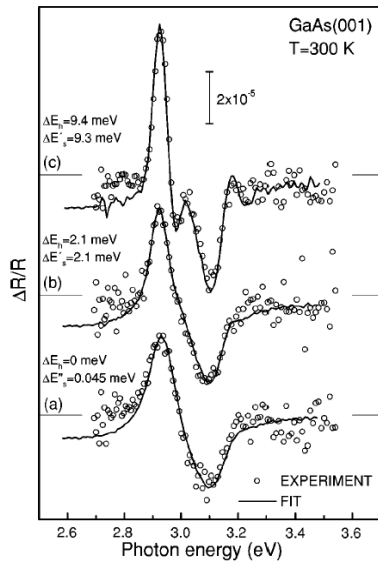


Fig. 14. Photoreflectance difference spectra of GaAs (001) (open circles) for: a) no applied stress and stresses, b) $X = -1 \times 10^8 \text{ N/m}^2$, c) $X = -4.4 \times 10^8 \text{ N/m}^2$. Solid lines are the fits obtained using adequate formula. The hydrostatic and splitting energy shifts obtained from the fits are also presented (after Lastras-Martinez et al. [62])

The PRD spectra are presented in Fig. 14. The open circles were obtained by subtracting polarized from unpolarized PR spectra for GaAs without strain (the lower spectrum) and with applied stress (two upper spectra). The solid lines are fits to PRD spectra with formula proposed by Lastras-Martinez et al. The QEO term is well resolved for a stress of $X = -4.4 \times 10^8 \text{ N/m}^2$ and, in fact, it dominates the PRD spectrum. From the fitting to the PRD spectra, Lastras-Martinez et al. obtained the hydrostatic energy shifts $\Delta E_h = 2.1 \text{ meV}$ and $\Delta E_h = 9.4 \text{ meV}$, for the spectra in Figs. 14b and c, respectively, and, additionally, the splitting energy shifts $\Delta E'_s = 0.04 \text{ meV}$, $\Delta E'_s = 2.1 \text{ meV}$, and $\Delta E'_s = 9.3 \text{ meV}$ for the spectra in Figs. 14a–c, respectively.

The model proposed by Lastras-Martinez et al. [62] gives an excellent description of the evolution of the PRD spectra with a stress. The results presented give a further evidence that the PRD has its physical origin in a piezo-optic effect and help the development of PRD spectroscopy as a characterization tool of surface electric fields and piezo-optical properties of zinc blende semiconductors.

There is a number of reports on the PR investigations of strain effects in various material systems including: $\text{In}_x\text{Ga}_{1-x}\text{As}/\text{GaAs}$ [64], $\text{In}_x\text{Ga}_{1-x}\text{As}/\text{InP}$ [52], $\text{In}_x\text{Ga}_{1-x}\text{As}/\text{Al}_{0.28}\text{Ga}_{0.72}\text{As}$ [65], InP/Si [66], ZnTe/GaAs [67], CdTe/GaAs [68], GaN on different substrates [69–74].

4.5. Built-in electric field

As was discussed earlier, the observation of the Franz–Keldysh oscillations in photorefectance spectra allows the determination of the built-in electric field in the sample. If the sample consists of one or more epilayers on the substrate, the superposition of two or more PR signals from different depths of the structure is probable. It is possible to have different values of the internal electric field at the surface or at a particular interface because of the difference in the density of surface and interface states. If we extract the FKO related to surface or interface, we can independently determine the electric fields.

There are a few methods of the decomposition of PR signal into the surface and interface related contributions. The first one uses the fact that we have two signals from different depths in the sample. In the case of PR signal consisting of two subsignals: from the surface region and from the interface one, the etching procedure changed only one part of the signal measured. The PR subsignal from the interface is changed due to the change in the distance between the surface and interface. For such a case we can write

$$\left(\frac{\Delta R}{R}\right)_1 = \left(\frac{\Delta R}{R}\right)_S + A\left(\frac{\Delta R}{R}\right)_I \quad (26)$$

$$\left(\frac{\Delta R}{R}\right)_2 = \left(\frac{\Delta R}{R}\right)_S + B\left(\frac{\Delta R}{R}\right)_I \quad (27)$$

where 1 and 2 represent the PR signals measured for as-grown sample and after etching, respectively, and S and I mean the signal from the surface and interface, respectively. Following the relations (26) and (27), we can determine the subsignal from interface as the difference between the spectra measured for as-grown and etched samples [75–77]. This subsignal is given with the accuracy of a constant factor. It is sufficient because PR spectra are usually given in arbitrary units. Plotted in Fig. 15 is the example of the PR spectra for $\text{GaAs}/\text{SI-GaAs}$ homojunction, before etching and

after two sequential etching procedures [76]. In Fig. 16, the decomposition into signals from the surface and from the interface is shown.

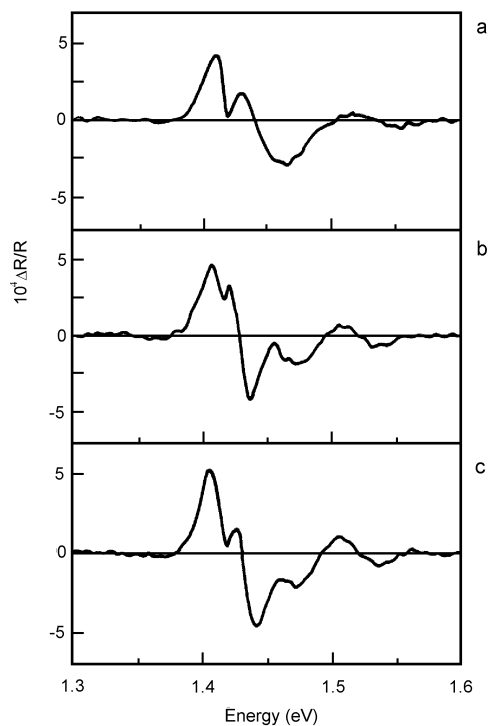


Fig. 15. PR spectra for an n-type GaAs/SI GaAs structure: a) before etching, b) after etching for 1 min, c) after next etching for 1 min (after Jezierski et al. [76])

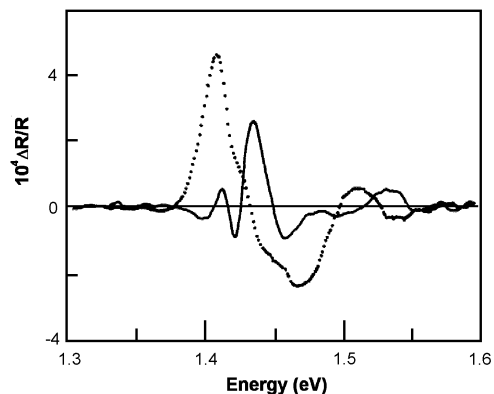
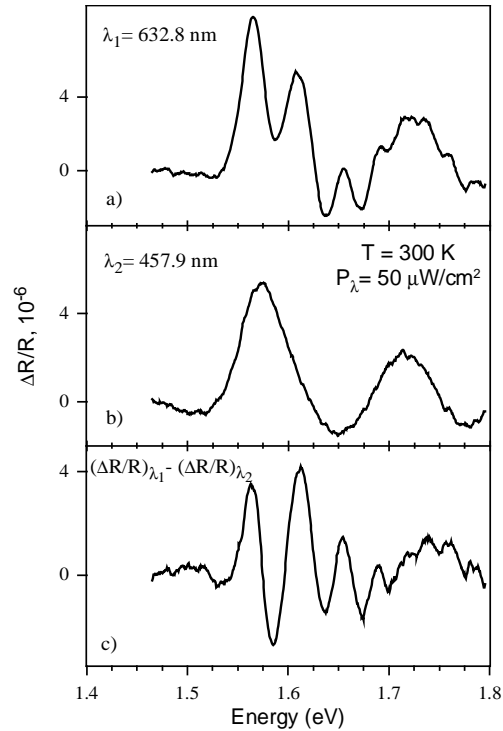


Fig. 16. PR spectra determined by the decomposition of the spectra shown in Fig. 14 into spectrum connected with the internal electric field in the surface region (dotted line) and the spectrum connected with the internal electric field in the interface region (solid line) (after Jezierski et al. [76])

An analogous method may be used in a non-destructive mode when the etching procedure is replaced by two PR measurements with two different wavelengths of the laser pump beam [32, 78–81]. In this case, the situation can be even simpler. If one of the spectra is measured using a very short wavelength of the laser, the signal comes only from the surface (parameter A in Eq. (26) is equal to zero). Then the subsignal from the interface can be obtained by taking the difference between PR signals obtained with longer and shorter laser wavelengths. The example of application of this method is shown in Fig. 17 for the case of $\text{Al}_{0.11}\text{Ga}_{0.89}\text{As}$ layer grown on GaAs substrate [32].

Fig. 17. PR spectra for $\text{Al}_{0.11}\text{Ga}_{0.89}\text{As}$ layers obtained with using the following pump beams: a) 632.8 nm line of the He-Ne laser; b) 457.9 nm line of the Ar^+ laser; c) the difference between the two former spectra giving the Franz–Keldysh oscillations connected with the electric field at the $\text{Al}_{0.11}\text{Ga}_{0.89}\text{As}/\text{GaAs}$ interface (after Sitarek et al. [32])



Another method of evaluating internal electric fields from the photoreflectance is the fast Fourier transformation (FFT) of the PR spectrum [82–88]. FFT is applied to the PR spectra in the energy region higher than the band gap energy to obtain the FKO period and then the electric field in the sample.

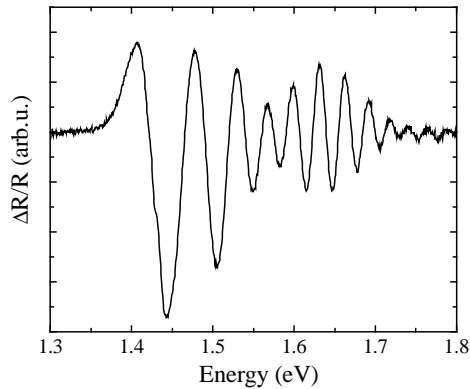


Fig. 18. Room-temperature PR spectrum of the δ -doped GaAs layer (after Nowaczyk et al. [88])

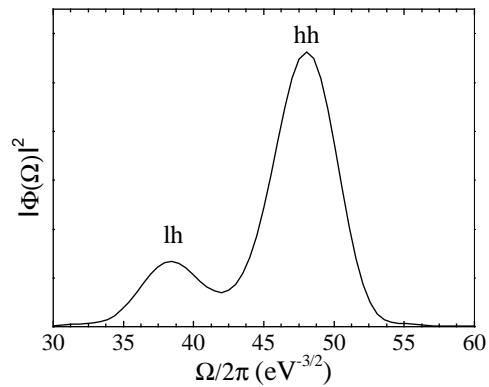


Fig. 19. Fast Fourier transform of the PR spectrum from Fig. 18 (after Nowaczyk et al. [88])

Nowaczyk et al. [88] investigated silicon delta doped (approx. $1 \times 10^{12} \text{ cm}^{-2}$) GaAs MOVPE-grown layers on undoped GaAs substrate. Figure 18 shows the PR spectrum

for this δ -doped sample. A lot of well-distinguished Franz–Keldysh oscillations (more than 20 extrema) above the GaAs band gap energy are seen, demonstrating the existence of a strong uniform electric field in a high quality epitaxial layer. Fast Fourier transform has been applied to this PR spectrum in the energy region higher than the band gap to obtain the FKO period and then the internal electric field. Prior to the Fourier transformation, the experimental PR spectrum was renormalized. A new argument $z = (E - E_g)^{3/2}$ was chosen and then the spectrum was multiplied by $E^2(E - E_g)$ in order to deal with periodic functions and compensate the inherent damping of FKO, respectively. Then the Fourier transform of a new function

$$\gamma(z) = \frac{\Delta R}{R}(z)(E - E_g)E^2 \quad (28)$$

is calculated as follows

$$\Phi(\Omega) = \int_{z_1}^{z_2} \gamma(z) \exp(-i\Omega z) dz \quad (29)$$

where $z_1 = (E_1 - E_g)^{3/2}$ and $z_2 = (E_2 - E_g)^{3/2}$ are the left and right boundaries of the window for the Fourier transform. The frequency Ω is directly related to the magnitude of the electric field by

$$\Omega = \frac{4}{3(\hbar\Theta)^{3/2}} = \frac{4\sqrt{2}}{3\hbar q} \frac{\sqrt{\mu}}{F} \quad (30)$$

where $\hbar\Theta$ is defined by Eq. (3). The square of the modulus of the complex Fourier transform is plotted in Fig. 19. Ideally, each built-in electric field should produce two peaks in the FFT corresponding to light hole (lh) and heavy hole (hh) channels of the optical transitions, which is seen in our case.

The width of the peak is inversely proportional to the window selected for the FFT, i.e. to the range of the original PR spectrum. The built-in electric field determined for the GaAs sample, for both heavy and light hole frequencies, is 53 kV/cm. This allowed determining the potential barrier height V_B between the surface and the δ -doped region of the sample. The value of the potential barrier was found to be 0.74 V.

4.6. Influence of annealing, processing and growth

Photoreflectance spectroscopy has become an effective tool to study various process- and growth-induced effects [78, 79, 89–100]. Ga(As,N) presents a new class of semiconductors which are promising materials for optoelectronic devices such as lasers and detectors operating at 1.3 and 1.55 μm . In such an alloy the band structure decreases dramatically due to N incorporation.

Klar et al. [99] used the PR spectroscopy to study the electronic and lattice properties of $\text{GaN}_x\text{As}_{1-x}$ epitaxial layers before and after hydrogenation. Five $\text{GaN}_x\text{As}_{1-x}$ epitaxial layers with $x = 0.00043, 0.00095, 0.0021, 0.005, \text{ and } 0.019$ and the thickness of $0.5 \mu\text{m}$ were grown on (100) GaAs substrates by MOVPE technique. The samples are unintentionally n-type doped. Pieces of all samples were hydrogenated by ion-beam irradiation from a Kaufman source with the sample temperature held at 300°C .

Figure 20 shows the PR spectra of a $\text{GaN}_x\text{As}_{1-x}$ epitaxial layer with $x = 0.005$ before and after hydrogenation, together with the GaAs reference spectrum. The PR spectrum after hydrogenation shows the shift of the E_- band gap toward that of GaAs. The corresponding $E_- + \Delta_0$ band exhibits a comparable blue shift. The E_+ feature disappears after hydrogenation.

The energy positions of the three signals before and after hydrogenation are summarized in Fig. 21. The solid lines are the fit of the level repulsion model to the experimental data. The dashed horizontal lines indicate the position of E_- and $E_- + \Delta_0$ in GaAs.

Fig. 21. Energy positions vs. N concentration x of the direct band gap E_- , the spin-orbit split-off band $E_- + \Delta_0$ and the N-induced E_+ band of the as-grown $\text{GaN}_x\text{As}_{1-x}$ samples (full circles). The solid lines are the fit of the level repulsion model to the experimental data. Corresponding data for E_- and $E_- + \Delta_0$ of the hydrogenated samples (open squares); there is no E_+ signal after hydrogenation. The dashed horizontal lines indicate the position of E_- and $E_- + \Delta_0$ in GaAs. $T = 300 \text{ K}$ (after Klar et al. [99])

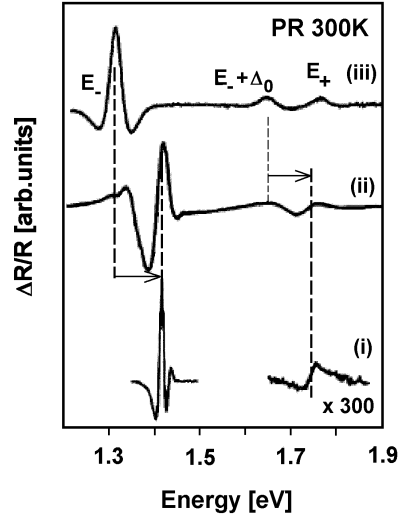
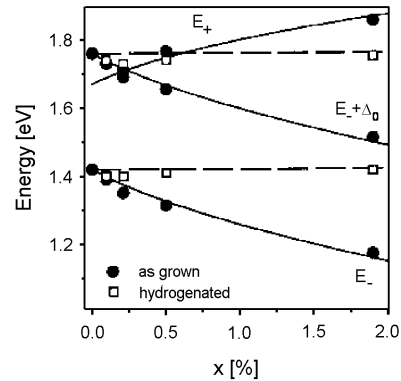


Fig. 20. PR spectra taken at $T = 300 \text{ K}$ of GaAs (i), $\text{GaN}_{0.005}\text{As}_{0.995}$ (ii) after hydrogenation, and $\text{GaN}_{0.005}\text{As}_{0.995}$ (iii) as grown (after Klar et al. [99])



Klar et al. [99] found that hydrogenation leads to an effective removal of the N-related perturbation due to the formation of a NH-complex. Hydrogenation literally reverses all the effects of N on the band structure of the GaAs host.

The influence of the carrier localization on modulation mechanism in photoreflectance of GaAsN and GaInAsN was investigated by Kudrawiec et al. [100]. They recorded the photoreflectance spectra of as-grown layers of GaAsN and GaInAsN from

10 to 300 K. Different modulation intensities and laser beam wavelengths were used. For the interpretation of PR data, the Kramers–Kronig analysis was employed. Kudrawiec et al. observed a decrease in PR signal with decreasing temperature and attempted to explain such a behaviour (observed by others as well) for the first time. They explain the above-mentioned effect as a weakening of the modulation efficiency induced by the carrier localization that has been evidenced earlier in alloys with diluted nitrogen.

5. Photoreflectance study of low-dimensional semiconductor structures

5.1. Quantum wells

Since the middle of sixties, the modulation spectroscopy techniques have proved their high applicability for studying and characterizing properties of bulk semiconductors. During the first decade, the method was recognized as a new, high-resolution technique for the solid state spectroscopy [13, 15, 101].

In the eighties, the modulation spectroscopy had a renaissance. The advantages exploited for bulk studies were applicable also in the semiconductor microstructures fabricated by MBE or MOCVD such as quantum wells (QWs), multiple quantum wells (MQWs) or superlattices (SLs). In 1985, Glembocki et al. [1] showed that multiple quantum wells, grown on semi-insulating substrates, could be studied by the photoreflectance technique.

Lineshape analysis, based on Eqs. (4), (14) and (15) (we will call it further fitting procedure) is an integral aspect of the photoreflectance spectroscopy. These procedures allow analysing complicated photoreflectance spectra in terms of theoretical parameters. Thus, the fitting provides valuable information about the energy gaps and linewidths associated with the optical transitions.

Photoreflectance spectra (dotted lines) of a GaAs/AlGaAs MQW structure (with the well width of 20 nm) at the temperatures of 6 K, 77 K and 150 K in the region of the 11H and 11L features [6, 21] are shown in Fig. 22. The solid and dashed lines are fits to the first-derivative of Lorentzian (first derivative Lorentzian lineshape – FDLL) and Gaussian (first derivative Gaussian lineshape – FDGL) profiles, respectively. At 6 K, the fit of the Lorentzian profile to the data is very good. At 77 K, the data cannot be adequately represented by either profile. An intermediate profile is required to fit the data. A Gaussian dielectric function results in a nearly perfect fit at 150 K.

For quantum wells, because of the enhanced exciton binding energy caused by the reduced dimensionality, the dielectric function has an excitonic character even at elevated temperatures, where the dielectric function broadening, caused by strong exciton–phonon interaction, impurities and defects, changes the absorption profile of excitons

from Lorentzian to Gaussian. Thus, at high temperatures, the Gaussian profile of the dielectric function must be used to fit the experimental data. At low temperatures, the Lorentzian dielectric function is more appropriate. Between 50 K and 150 K the transition from the Lorentzian to Gaussian profile is not abrupt and the lineshapes are of an intermediate form between Lorentzian and Gaussian. Equation (4) with the parameter $m = 3$ (2D critical point) sometimes is used to reflect the FDGL, providing a reasonable fit to the room-temperature experimental data.

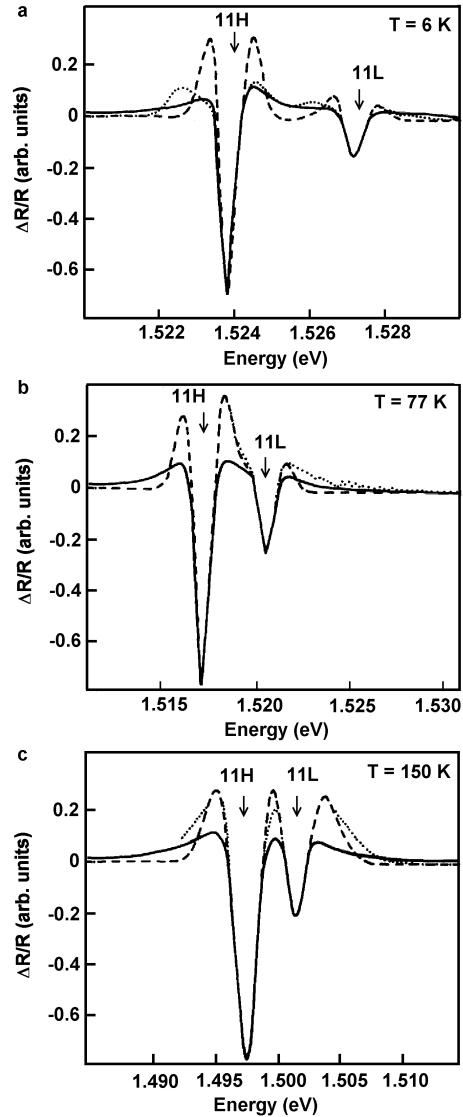


Fig. 22. Photoreflectance spectra (dotted line) at different temperatures from a GaAs/AlGaAs MQW structure. First-derivative Lorentzian (solid lines) and Gaussian (dashed lines) lineshapes are compared (after Glembocki [6])

At the beginning, single QW or MQW structures received most attention in PR studies. In MQW structures, the barrier layer is thick enough to prevent any significant wave function overlap between wells.

In addition to parity-allowed transitions ($m - n = 0, \pm 2, \pm 4, \dots$), it has been shown that parity-forbidden transitions can be observed in QWs. The selection rules may be broken, i.e. by nonparabolicities in the valence band states and by electric field (internal and external).

Allowed and forbidden optical transitions in a GaAs/AlGaAs MQW structure were studied by Sitarek et al. [102]. The structure was grown by the MBE on (001) GaAs substrate. The MQW under investigations consisted of 60 periods of GaAs and $\text{Al}_{0.35}\text{Ga}_{0.65}\text{As}$ layers, each 15 nm thick. The PR spectrum measured at room-temperature had a very rich structure. In order to identify all features, a PR measurement was also carried out at a liquid nitrogen temperature. The PR spectrum obtained is shown in Fig. 23.

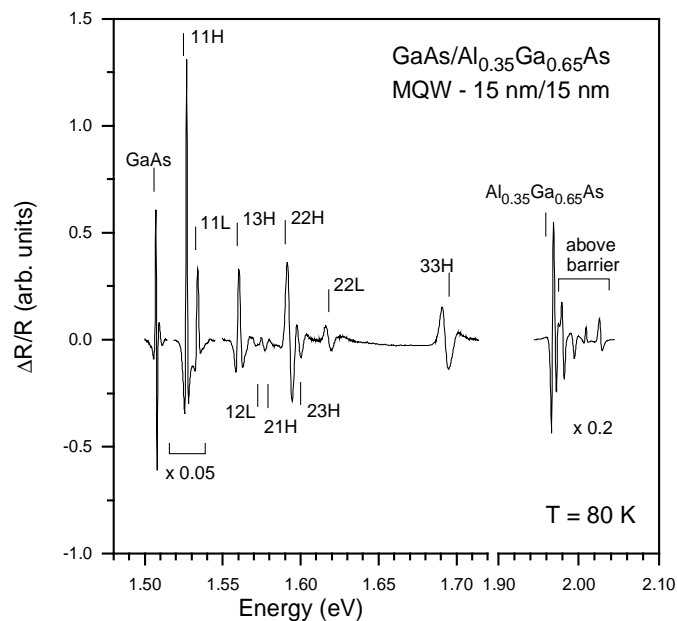


Fig. 23. Photoreflectance spectrum of GaAs/ $\text{Al}_{0.35}\text{Ga}_{0.65}\text{As}$ MQW with wells and barriers of 15 nm width measured at 80 K. The vertical lines indicate optical transition energies obtained from the theoretical calculation (after Sitarek et al. [102])

The vertical lines indicate intersubband transitions. Both, the symmetry-allowed and symmetry forbidden transitions are marked in the figure. A small, built-in electric field is probably responsible for the presence of 21H, 23H and 21L symmetry-forbidden transitions in the spectrum, which are much weaker than the symmetry-allowed ones. Because of the finite depth of the well, the 13H transition is parity allowed and its in-

tensity is comparable to the symmetry-allowed transitions. Optical transitions involving unconfined states are present above the feature corresponding to the band gap of Al-GaAs [103]. The energies of resonances present in the spectrum were accurately determined by Sitarek et al. through the fit of the first derivative Gaussian lineshape function (14) to the experimental data.

In order to identify the nature of the large number of intersubband transitions observed in the MQW, Sitarek et al. have performed a theoretical calculation based on the envelope function approximation [104]. The energy values obtained from this calculation agree very well with the experimental data.

The temperature dependence of both the energy and broadening of interband electronic transitions can yield important information about, e.g. electron-phonon interactions or excitonic effects. An increase of temperature leads to a red shift of the band gaps and an increase in the linewidth. The temperature variation of the energy gaps can be described by equations involving three parameters such as the Varshni expression or the more recently proposed term containing the Bose-Einstein occupation factor for phonons (Eqs. (18), (19)) [3]. A similar Bose-Einstein equation has also been used to fit the temperature dependence of the broadening function (Eq. (20)).

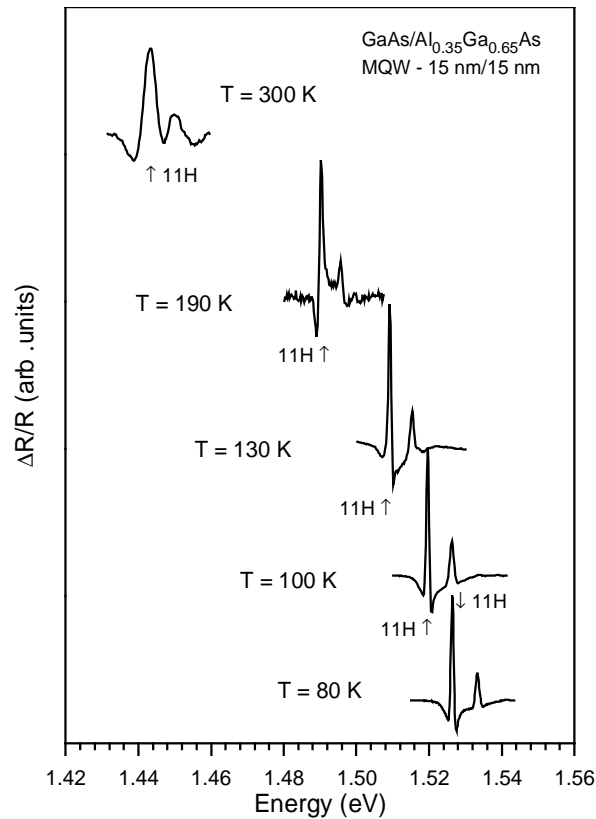


Fig. 24. The photoreflectance spectra of GaAs/Al_{0.35}Ga_{0.65}As MQW structure in the energy range of 11H and 11L transitions measured at different temperatures. Their intensities are not in scale. Arrows mark 11H transition energy (after Sitarek et al. [102])

Sitarek et al. [102] have reported a study of the temperature dependence of PR spectra from $\text{Al}_{0.35}\text{Ga}_{0.65}\text{As}/\text{GaAs}$ MQW in the 80–300 K temperature range. In Fig. 24, the PR spectra of the 11H and the 11L transitions at different temperatures are shown. From the least-squares fits to the experimental data with FDGL, the values of $E_{11\text{H}}$ were obtained. The fit also yielded the broadening parameter Γ .

The parameters in the Bose–Einstein expression such as the strength of the electron–phonon interaction a_B , and Θ_B corresponding to the average phonon temperature, (see Eq. (19)) describe the temperature dependence of 11H transition energies of $\text{AlGaAs}/\text{GaAs}$ MQW. The values of a_B and Θ_B obtained for 11H transition are very similar to the values for bulk GaAs. In the lattice matched $\text{AlGaAs}/\text{GaAs}$ heterostructures, the temperature dependence of the band gap of the material forming the wells is the main factor affecting the relation of the transition energy and temperature.

The variation of the broadening parameter with temperature can also be expressed by the Bose–Einstein expression (see Eq. (20)). Parameter Γ_0 contains inhomogeneity contribution resulting from the interface roughness, alloy clustering and strain distribution (a small value of Γ_0 tells us that structure is very homogeneous). For the 11H transition, Sitarek et al. [102] found that $\Gamma_0 = 0.71$ meV.

In the studies of electronic and optical properties of quantum wells (and multiple quantum wells), the major attention was focused on confined states. In quantum well structures, the existence of energy levels formed above (below) the conduction (valence) band of the barriers has been observed in both low-temperature Raman spectroscopy [105] and low-temperature PLE spectroscopy [106]. Using photoreflectance spectroscopy, it is possible to investigate optical transitions involving unconfined states at room temperature [107, 108]. Up to now little work has been done on the study of such subbands.

The features observed at the energies higher than the resonance corresponding to bulk AlGaAs seen in Fig. 23 were under detailed study by Sitarek et al. [103]. A room-temperature PR spectrum for a $\text{Al}_{0.35}\text{Ga}_{0.65}\text{As}/\text{GaAs}$ MQW with a 15 nm well width, is shown in Fig. 25 for the energies equal and higher than the band gap of the barrier energy. The feature at about 1.87 eV corresponds to the direct band gap of AlGaAs . Three additional features, marked A, B and C, were observed above the resonance related to AlGaAs band gap.

Sitarek et al. [103] reported energy level splitting in the optical transitions between unconfined electron and hole subbands in $\text{AlGaAs}/\text{GaAs}$ MQWs. The splitting is associated with the energy dispersion in the direction along the MQW growth direction (z -axis). This dispersion leads to the formation of subbands in superlattices (and MQW structures). The width of the subband is determined by the energy difference between the quantized state at $k_z = 0$ (Brillouine zone centre) and $k_z = \pi/d$ (Brillouine zone edge). Here $d = L_W + L_B$ is the sum of the well thickness L_W and the barrier thickness L_B .

In order to obtain the transition energies between subbands, the third-derivative functional form (Eq. (4)) [109, 15] was used to fit the PR experimental data. The solid line in Fig. 25 shows the least squares fit to the TDFP.

The quasibound states at the above-barrier region in type-II ZnTe/CdSe superlattices were observed at room temperature by photoreflectance, contactless electroreflectance, as well as photoconductivity measurements by Tseng et al. [110]. They provide a concrete evidence for the strong localization of the carrier waves in the barrier region. It was found that the barrier-width dependence of the above-barrier ground-state transition energies can be well described by the constructive interference condition. Tseng et al. observed the absorptive spatially indirect transition between electrons confined in the CdSe and holes confined in the ZnTe layers.

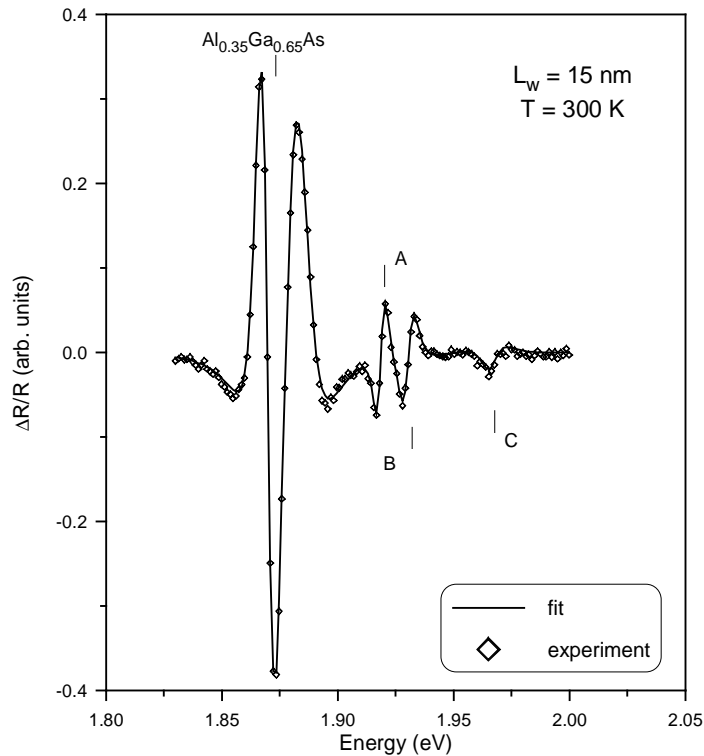


Fig. 25. Photoreflectance spectrum of GaAs/ $\text{Al}_{0.35}\text{Ga}_{0.65}\text{As}$ MQW structure in the range above the barrier transitions. Solid line is the fit according to Eq. (4). Vertical lines mark the energies of optical transitions involving unconfined states (after Sitarek et al. [103])

In strained systems, the properties of the electron and hole quantum states depend on both the strain and quantum confinement. It is useful to define the conduction band offset parameter

$$Q_C = \frac{\Delta E_C}{\Delta E_C + \Delta E_V^{HH}} \quad (31)$$

where ΔE_C and ΔE_V^{HH} are the conduction band and the heavy-hole valence band discontinuities, respectively. When thin InGaAs layers are grown on a AlGaAs buffer layer, a biaxial in-plane compression and a corresponding extension (tensile strain) along the growth direction are sustained in InGaAs. Such a strain alters the band structure of InGaAs [111]. The energy band gap increases due to the compressive hydrostatic component of the strain while the tensile, (001) uniaxial strain splits the heavy-light hole degeneracy at the Brillouine zone centre. The relative positions of the bands in the InGaAs/GaAs QWs can lead to two possible configurations of the potential of the well. If the conduction band offset parameter Q_C is less than 0.5, both the electrons and the holes are confined to the InGaAs region. In the other case ($Q_C > 0.5$), the electrons and the heavy holes are in the InGaAs region (configuration of type I), while the light holes are in the GaAs region (configuration of type II).

Søk et al. [112] studied the InGaAs/GaAs QW structure grown by MOCVD. The structure consisted of five 10 nm $\text{In}_{0.115}\text{Ga}_{0.885}\text{As}$ quantum wells separated with 80 nm GaAs barriers. They also concluded that light holes are confined in GaAs layer configuration of type II.

Because of their potential applications for long-wavelength optoelectronic devices, e.g. high-performance laser diodes emitting at the 1.3 and 1.55 μm optical fibre window, narrow band-gap semiconductors and especially low-dimensional structures based on such semiconductors are widely investigated.

A recent increase in interest in QW structures operating in the 1.3–1.55 μm spectral region caused an increase in applications of the post-growth techniques that produce non-square QWs, for the modification of the operation wavelength of well-known InP-based laser structures. The InGaAsP/InP laser structures grown by gas source MBE have been investigated by Kudrawiec et al. [113]. The structures were modified using the rapid thermal annealing (RTA) technique. The migration of atoms across quantum well interfaces (during RTA) changes the quantum well profile from a square to a rounded well and is responsible for that blue shift (in comparison to as-grown structure) of all optical transitions observed in PR. Thus using RTA (or other techniques) enables tuning the laser structure to a proper wavelength.

Another alloy which may be used for the construction of long-wavelength optoelectronic devices is the quaternary alloy InGaAsN. Compared to the InGaAsP quantum well system, GaInAsN/GaAs QW's have a larger conduction band offset which leads to a stronger electron confinement and hence higher characteristic temperatures. The high-temperature performance of GaInAsN-based laser diodes is expected to be better than that of InGaAsP devices. Due to its possible applications GaInAsN/GaAs QWs have been widely investigated in recent years (see for example [114–119]).

The $\text{In}_x\text{Ga}_{1-x}\text{Sb}/\text{GaSb}$ strained system has potential applications for example in: trace gas sensing, atmospheric pollution and drug monitoring, medical procedures such as laser surgery and medical diagnostic, absorption spectroscopy or long-haul telecommunications, and especially low threshold current lasers at wavelengths ranging from 1.5 to 2.2 μm .

Single quantum well $\text{In}_{0.22}\text{Ga}_{0.78}\text{Sb}/\text{GaSb}$ structure grown by MBE on GaSb substrate was investigated by Kudrawiec et al. [120]. Figure 26 shows a comparison of photoluminescence, reflectance, photorefectance, transmittance and phototransmittance spectra of a $\text{In}_{0.22}\text{Ga}_{0.78}\text{Sb}/\text{GaSb}$ single quantum well recorded at $T = 10$ K. In the PL spectrum, three peaks are observed. Two high-energy peaks (at 0.776 and 0.790 eV) are GaSb defect-related and were previously observed in GaSb-based quantum well structures. The third, dominating, very narrow (3.5 meV) peak at 0.691 eV, labelled 1C-1HH, originates from the quantum well and represents ground-state heavy-hole exciton radiative recombination. In reflectance spectrum only a feature associated with GaSb band gap exciton (in the buffer and/or cap layer) is clearly observed. Only a very weak trace of the quantum well-related signal is seen. On the contrary, strong and well-resolved features are observed in the photorefectance and phototransmittance (PT) spectra below the GaSb band gap energy.

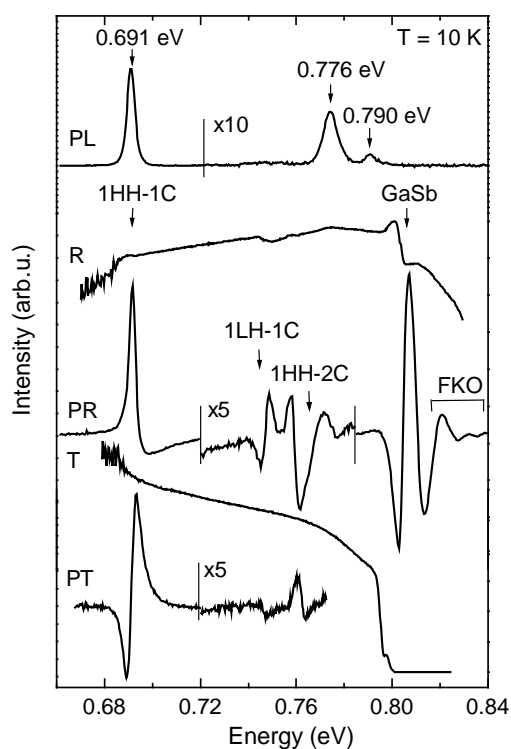


Fig. 26. Comparison of photoluminescence (PL), reflectance (R), photorefectance (PR), transmittance (T) and phototransmittance (PT) spectra of $\text{In}_{0.22}\text{Ga}_{0.78}\text{Sb}/\text{GaSb}$ single quantum well at 10 K (after Kudrawiec et al. [120])

Due to the transparency of the GaSb substrate for light of wavelengths longer than $1.55 \mu\text{m}$ (at 10 K), it was possible to carry out the photomodulation spectroscopy experiments in reflection and transmission modes and both techniques appeared to probe the single $\text{In}_{0.22}\text{Ga}_{0.78}\text{Sb}$ quantum well. In both derivative spectra (PR and PT), the same quantum well-related transitions are observed. There is only one important difference between photoreflectance and phototransmittance and hence also between their spectra. In PR, a strong GaSb-related feature is seen in the shape of the Franz–Keldysh oscillations, reflecting the existence of a weak built-in electric field at the surface of GaSb or at GaSb buffer–GaSb substrate interface. It is impossible to observe such a signal in PT spectrum due to the strong absorption in the GaSb substrate which starts to increase significantly when the photon energy of the probe beam approaches the energy of GaSb band gap (0.8 eV).

In terms of device applications, wide band-gap semiconductors are very important, especially for so-called “blue optoelectronics”. Wetzal et al. [121, 122] have performed enhanced studies of multiple quantum well $\text{In}_x\text{Ga}_{1-x}\text{N}/\text{GaN}$ systems using photoreflectance spectroscopy.

As long as the barriers in multiple quantum wells structure are thick, the coupling between the wells does not occur. The simplest structure containing coupled QWs is double quantum well (DQW). Sk et al. [123] studied undoped symmetric structure with two GaAs/AlGaAs quantum wells separated by an AlAs mono-layer (ML). The structure was grown by the MBE on a (001) semi-insulating GaAs wafer. In Fig. 27, a room-temperature PR spectrum for the investigated structure is shown. A few resonances related to DQW transitions occur above the feature related to GaAs band gap transition. The transitions are labelled according to the common notation with indices s and a , where index s (a) means the transition between symmetric (antisymmetric) states. Sk et al. [123] obtained a very good agreement between the experimental transition energies and those from theoretical calculations based on envelope function approximation.

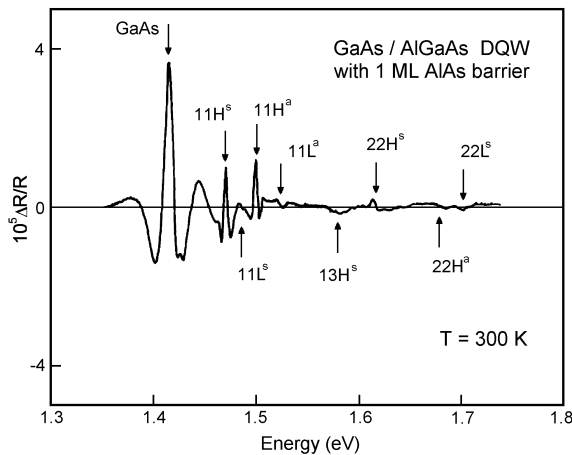


Fig. 27. Photorefectance spectrum from the GaAs/Al_{0.3}Ga_{0.7}As double quantum well structure. Arrows indicate the experimental transition energies (after Sk et al. [123])

The In_{0.045}Ga_{0.955}As/GaAs DQW structure was investigated by Sk et al. [124]. They examined the dependence of the intensity of forbidden transitions on the built-in electric field. To change the electric field in the structure, the authors used an additional laser beam (third light beam). They found that the ratio of the intensity of forbidden transitions to the intensity of the fundamental allowed transition depends linearly on the third beam power density and hence approximately linearly on the internal electric field in the region of DQW.

To obtain an enhanced spatial resolution comparing to conventional PR, Cho et al. [125] put forward the near-field scanning optical spectroscopy combined with PR to investigate Al_{0.3}Ga_{0.7}As/GaAs quantum well structures.

5.2. Quantum dots

With nanoscale lithographic techniques used to 2D heterostructures, it is possible to obtain quantum dots (QD) – quasi zero dimensional (0D) objects.

Qiang et al. [126] reported room-temperature PR studies of GaAs/Ga_{0.7}Al_{0.3}As quantum dots arrays, fabricated by reactive ion etching. An MBE structure, consisting of a 500 nm of an unintentionally doped GaAs buffer layer followed by 100 periods of GaAs(8 nm)/Ga_{0.7}Al_{0.3}As(12 nm) quantum wells, capped by 10 nm of GaAs, was grown on (001) semiinsulating GaAs substrate. Three quantum dot arrays, with the lateral sizes of 500 nm, 400 nm and 230 nm, and MQW control structure have been investigated. The distance between the dots was four times greater than their diameter.

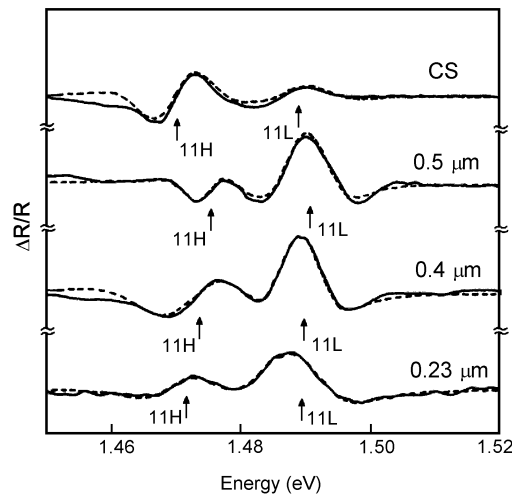


Fig. 28. Photoreflectance spectra at 300 K in the region of 11H and 11L transitions from three GaAs/Al_{0.3}Ga_{0.7}As quantum dot arrays and the spectrum of the control structure (after Qiang et al. [126])

The solid lines in Fig. 28 show room-temperature photoreflectance spectra of the control sample and the QD arrays. The dashed lines are the least-square fits of the data to the first derivative of a Gaussian profile. The calculations yield the energy positions and the broadening parameters of PR features. Energies of 11H and 11L optical transitions obtained from the experiment are denoted by arrows.

The energy positions of 11H and 11L from the control sample are consistent with an 8 nm GaAs quantum well. The energy of the 11L transition varies very little from sample to sample. When compared to the control sample, the energy of 11H optical transition in the 500 nm dot structure is blue shifted by about 5 meV. It decreases to almost its original position (in the control sample) in the 230 nm dot array. The strain induced by RIE is fairly uniform resulting in small differences in the broadening parameters for all resonances.

Qiang et al. explained the behaviour of 11H and 11L transition energies in terms of the strains in the quantum dots. For the 500 nm dots there is a compressive strain of about -7×10^{-4} along the growth direction. A reduction of strain was observed when the lateral dimension of QD decreased. For the structure with the smallest dots the strain was reduced to about -2×10^{-4} .

Gumbs et al. [127, 128] investigated the intersubband transitions from modulation-doped GaAs/GaAlAs quantum dot arrays fabricated by RIE. By using PR performed at 77 K and 300 K, they studied two quantum dot structures with dots of 60 nm and 100 nm in diameter.

Klar et al. [129] investigated high-density patterns of ZnTe/Zn_{0.93}Mn_{0.07}Te quantum dots. Quantum dots with the diameter of 200 nm were prepared by electron lithography followed by Ar⁺ ion beam etching from four MBE grown ZnTe/Zn_{0.93}Mn_{0.07}Te MQW structures with 4 nm, 6 nm, 8 nm and 10 nm well widths. Photoreflectance measurements were performed at 10 K. The modulation was carried out with a 632.8 nm (1.96 eV) He-Ne laser (below-bandgap photomodulation). Klar et al. showed that the main effect of the nanofabrication process is a change in the strain of the quantum dot structures when compared with control sample. The parent structure is, in a good approximation, strained to the ZnTe buffer layer whereas quantum dots are unstrained.

For light hole excitons, an increase in the oscillator strength was observed in the QD structures. An electric dipole moment, parallel to the growth direction, introduced by the probe light that can penetrate the QD side walls (the side walls are not perpendicular to the surface) is a possible explanation of this effect.

Klar et al. [129] did not observe any confinement effects due to the reduction of the dimensionality from 2D to 0D. The lateral sizes of dots being under study were too large to observe such confinement effects.

The quantum dot structures, described in the above papers, were obtained by the lithography followed by etching processes. The size of dots and the level of perfection in such structures are limited by the lithographic processing. Using an epitaxial growth of materials with a large lattice mismatch is a way of obtaining islands of small lateral sizes of one material grown on the other material. Quantum dots obtained in such a way are referred as “self-assembled” or “self-organised”.

Ulrich et al. [130] used the above method to obtain nanoscale InP islands embedded in $\text{In}_{0.48}\text{Ga}_{0.52}\text{P}$ matrices. The structures were grown by MBE on (001) GaAs substrate. The substrate layer was followed by 200 nm of $\text{In}_{0.48}\text{Ga}_{0.52}\text{P}$ and from three to ten monolayers of InP, covered by another 200 nm $\text{In}_{0.48}\text{Ga}_{0.52}\text{P}$ cap layer. The atomic force microscope (AFM) pictures showed that the island density is of the order of 10^{10} cm^{-2} . This structure, with nominally three monolayers of InP, formed dots (islands) of 20–30 nm in diameter and 5–10 nm high. When the number of monolayers increases to seven, the dot diameter increases up to 40–50 nm.

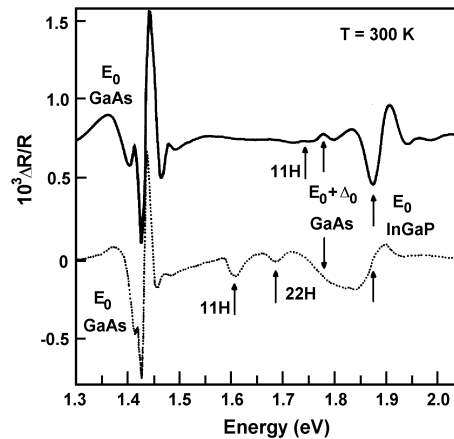


Fig. 29. Photoreflectance spectra of $\text{InP}/\text{In}_{0.48}\text{Ga}_{0.52}\text{P}$ island (dot) structures with 3 ML (solid line) and 7 ML (dashed line) of nominal InP thickness (after Ulrich et al. [130])

Figure 29 presents photoreflectance spectra, measured at 300K, for structures with three and seven monolayers of InP, respectively. Both spectra show resonances corresponding to $E_0(\text{GaAs})$, $E_0+\Delta_0(\text{GaAs})$ and $E_0(\text{InGaP})$ optical transitions. The transition denoted as 11H is an optical transition between the first heavy hole and the electron states of the InP islands. For the three-monolayer sample, the 11H transition is partially obstructed by the PR feature of $E_0+\Delta_0(\text{GaAs})$ transition. The transition labelled 22H is observed in the PR spectrum of the seven-monolayer sample. Ulrich et al. [130] proposed a simple theoretical model, based on the envelope-function approximation, to calculate the subband energies. The transition energies, obtained from the theoretical considerations, agree well with energy values obtained from the experiment for the structures with InP nominal thickness between three and ten monolayers.

Søk et al. [131] used room-temperature photoreflectance spectroscopy to investigate optical transitions in MOCVD-grown, InAs/GaAs structures with self-organised quantum dots.

Tellurium-doped GaAs substrate was followed by the following layers: 100 nm GaAs buffer, 25 nm $\text{Al}_{0.3}\text{Ga}_{0.7}\text{As}$, 100 nm GaAs and 1.65 nm monolayer of InAs. A strong lattice mismatch between the latter two compounds induces the formation of InAs pyramids. The QD pyramids are covered by 1 nm layer of $\text{In}_{0.3}\text{Ga}_{0.7}\text{As}$. This structure was then covered with the 20 nm layer of GaAs, 25 nm of $\text{Al}_{0.3}\text{Ga}_{0.7}\text{As}$ and capped with 20 nm of GaAs. From the transmission electron microscope measurements, the diameter of the dots is in 10–12 nm range while the height is about 2.5–3 nm.

A room-temperature PR spectrum of the investigated QD structure is presented in Fig. 30 (circles). In the figure, we can see three groups of features related to quantum dots, InAs wetting layer and GaAs band gap, respectively. The features labelled QD1, QD2 and QD3 correspond to optical transitions in quantum dots. The resonances designated as WL1 and WL2 correspond to the 11H and 11L transitions in the step-shaped quantum well, formed in the InAs wetting layer and the $\text{In}_{0.3}\text{Ga}_{0.7}\text{As}$ layer covering the dots.

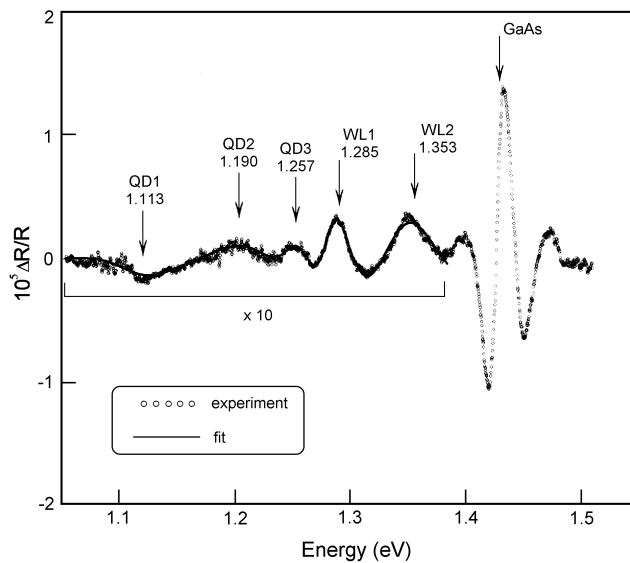


Fig. 30. Room-temperature PR spectrum of InAs/GaAs quantum dot structure (circles). Solid line represents a fit according to the first-derivative Gaussian lineshape to the experimental data. Arrows indicate the transition energies (after Sk et al. [131])

In order to obtain the transition energy values, fitting of the first derivative of the Gaussian lineshape to the experimental data was performed. The FDGL fit is presented in Fig. 30 as a solid line. The interpretation of QD related transitions was possible after theoretical calculations for buried, pyramid-shaped InAs QD's on (001) GaAs bound to {101} facets. Assuming the pyramidal shape of the dots, accounting for strain distribution, piezoelectricity, valence band mixing and conduction band–valence band coupling, the electronic structure and optical properties were modelled using 8-band $\mathbf{k}\cdot\mathbf{p}$ theory [104]. After extrapolating these results to room temperature

and taking into account the exciton binding energy, the values of transition energy are in good agreement with the experimental results. QD1, QD2 and QD3 transitions were identified as e_0-h_0 , e_2-h_1 and e_1-h_3 , respectively, where e_0 (h_0) denotes the ground electron (hole) state.

The vertical stacking of dots in laser structures and the idea of employing coupled dots in quantum computational concepts caused an increase of interest in the investigation of a dot-dot interaction in double dot systems. The photoreflectance turned out to be adequate also in this case. Sk et al. [132, 133] investigated three self-organized vertically coupled $\text{In}_{0.6}\text{Ga}_{0.4}\text{As}/\text{GaAs}$ double quantum dots structures differing only in the thickness L_s of the GaAs separating layer. The spectra of the structures obtained at 10 K PR are presented in Fig. 31.

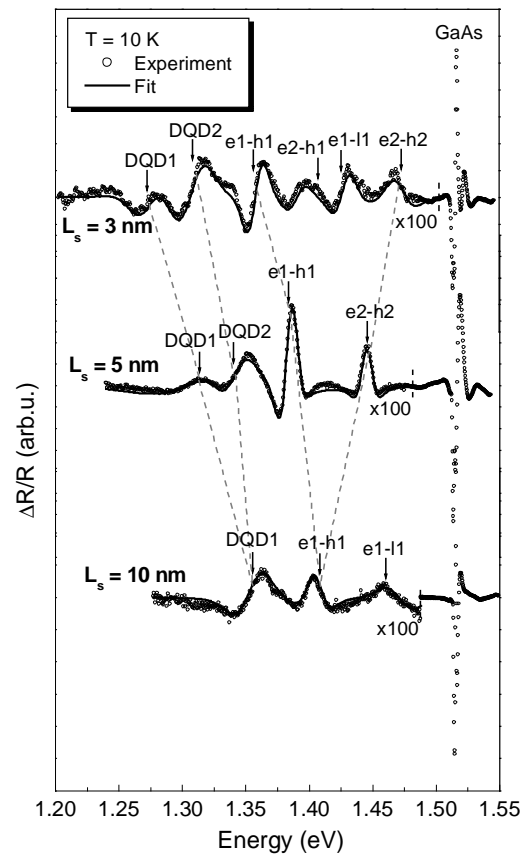


Fig. 31. Photoreflectance spectra of double quantum dot structures for various thicknesses of the separating GaAs layer (after Sk et al. [132])

The splitting of double wetting layer quantum well and quantum dot states due to the coupling has been observed even though the experiment was carried out on millions of dots and the PR lines were inhomogeneously broadened. The DQD's splitting energy has been determined from the experiment and compared to its calculated dependence on

the spacer thickness. A very good agreement was obtained which confirmed that for 10 nm thickness of the separating GaAs barrier the dots are almost uncoupled and structure can be treated as two independent layers of dots.

6. Photoreflectance study of device structures

In the preceding sections, it was shown that photoreflectance spectroscopy is a powerful tool for investigation of characteristic properties of bulk semiconductors and low-dimensional semiconductor heterostructures. The PR technique may be used not only for characterization of the low-dimensional structures but also to examine semiconductor device structures as well. In the next few paragraphs, we will present applications of PR spectroscopy for the studies of high electron mobility transistor (HEMT) structures, pseudomorphic HEMT (PHEMT) devices, heterojunction bipolar transistors (HBT), and vertical/planar light emitting lasers.

6.1. Transistors

A HEMT structure is formed by a charge transfer from a heavily doped AlGaAs layer to an undoped GaAs layer. This process results in placing the electrons in a very pure GaAs layer, resulting in very high electron mobility. A scheme of such a structure is shown in Fig. 32. The electrons transferred to the GaAs layer are confined to the interfacial region and form a two-dimensional electron gas (2DEG) in a nearly triangular potential well. In order to avoid Coulomb interactions between the electrons with enhanced electron mobility in 2DEG and the ionised donors in n^+ AlGaAs layer, an insulating AlGaAs spacer layer usually separates these two layers. The thickness of the spacer determines the number of electrons transferred. The presence of a potential well results in the formation of subband states in the conduction band. The valence band exhibits no confinement and hence has a three-dimensional characteristics.

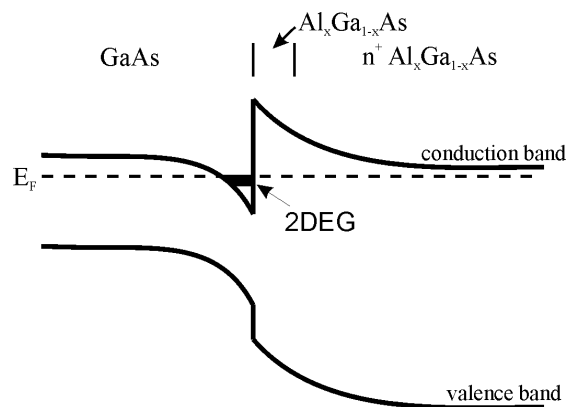


Fig. 32. Schematic diagram
of AlGaAs/GaAs HEMT structure

Soares et al. [134, 135] investigated three AlGaAs/GaAs HEMT structures with different spacer widths. All structures were grown by MBE on a semi-insulating GaAs substrate. The GaAs substrate was followed by 500 nm undoped active GaAs layer, an undoped $\text{Al}_{0.3}\text{Ga}_{0.7}\text{As}$ spacer, an Si-doped $\text{Al}_{0.3}\text{Ga}_{0.7}\text{As}$ barrier layer and an Si-doped GaAs cap layer of donor concentration $N_D = 3 \times 10^{18} \text{ cm}^{-3}$. The widths and donor concentrations of the barrier layers were 50 nm and $N_D = 1 \times 10^{18} \text{ cm}^{-3}$ for structure 1 and 40 nm and $N_D = 1.5 \times 10^{18} \text{ cm}^{-3}$ for structures 2 and 3, respectively. The thickness of the spacer layer was 0 nm, 6 nm and 8 nm.

Figure 33 presents room-temperature PR spectra of three HEMT structures. Each spectrum exhibits two types of oscillations: short-period oscillations at the fundamental gap of GaAs and wide-period oscillations extending over the whole spectral range. The wide-period oscillations originate from the Franz–Keldysh effect. The strength of the surface electric field, obtained from the period of FKO, is slightly lower than that obtained from the electric field profile calculations (about 750 kV/cm).

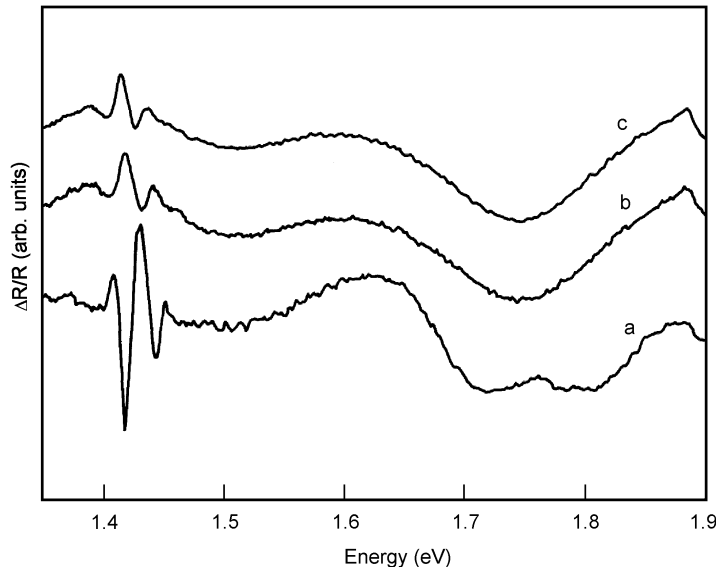


Fig. 33. Photoreflectance spectra from AlGaAs/GaAs HEMT structures 1 (a), 2 (b) and 3 (c) (after Soares et al. [134])

The short-period oscillations in structure 1 differ from oscillations in the other structures. For example, the amplitude of these oscillations for structures 2 and 3 is considerably smaller than for structure 1. The differences between structure 1 and the other structures, concerning GaAs layers, occur only at the AlGaAs/GaAs interfaces. Thus Soares et al. [134] attributed the lineshape discrepancies to different interface

qualities. In the case of sample 1, the interface is of relatively good quality and the charge density, associated with the interface defects, is small. Interface defects and the associated interface charge seem to be present in samples 2 and 3. The quality of the interface influences the electric field profile and hence the PR spectra. The short-period oscillations cannot be traced back to the Franz–Keldysh effect. Soares et al. assumed that the origin of these features is from optical transitions to subband states above the Fermi level. These subbands are formed in AlGaAs/GaAs potential well.

Søk et al. [136] studied two AlGaAs/GaAs HEMT structures grown by MBE. A buffer layer, 100 periods of GaAs(2.5 nm)/AlGaAs(2.5 nm) superlattice, 510 nm GaAs active layer, AlGaAs spacer layer of 40 or 80 nm width and 200 nm n-doped ($1 \times 10^{17} \text{ cm}^{-3}$) AlGaAs layer were grown on a GaAs substrate. The structure was terminated with a 17 nm GaAs cap layer.

A PR spectrum of HEMT structure with an 80 nm spacer layer is presented in Fig. 34. The spectrum can be divided into several independent regions. In the region around 1.42 eV, the main peak corresponds to GaAs band gap transition. A weak peak, visible in the low-energy part of this spectrum, is related to the excitonic transition. The additional resonance at 1.435 eV is probably related to a two-dimensional electron gas. Søk et al. [136] interpreted the oscillatory signal around 1.6 eV as the Franz–Keldysh oscillations associated with the superlattice (SL) present in the structure. In the presence of an internal electric field, the electrons can be accelerated in the field direction and transitions in short-period SL may be analyzed in terms of the miniband Franz–Keldysh effect. The electric field value, deduced from the period of the oscillations, is 4.4 kV/cm.

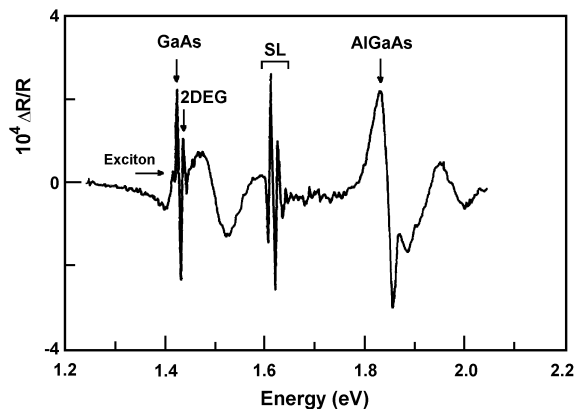


Fig. 34. Room-temperature spectrum from $\text{Al}_{0.33}\text{Ga}_{0.67}\text{As}/\text{GaAs}$ HEMT structure (after Søk et al. [136])

Between 1.45 eV and 1.6 eV there is a broad oscillation. Such an oscillation is characteristic of the Franz–Keldysh effect from the fully depleted GaAs cap layer. A feature corresponding to the AlGaAs band gap transition, appears in the spectrum

above 1.85 eV. From the position of this resonance, the Al content was deduced to be 33%. An additional feature is present at about 1.95 eV. This feature probably results from the overlapping of two Franz–Keldysh oscillations associated with AlGaAs band gap resonances from different parts of the structure: from the highly doped AlGaAs layer and the undoped AlGaAs spacer.

The photoreflectance spectrum obtained from the structure with a 40 nm spacer layer was very similar to the previous one. The only difference was in the absence of the excitonic feature due to the higher (6.3 kV/cm) electric field formed in this structure.

One type of HEMT, the pseudomorphic AlGaAs/InGaAs/GaAs modulation doped structure (PHEMT), demonstrated an outstanding power performance. In the AlGaAs/InGaAs/GaAs system, a large electron concentration in the two-dimensional gas can be achieved while the electron mobility remains very high. These structures promise device performance up to a few hundred GHz. The energy band profile of PHEMT structure is shown in Fig. 35.

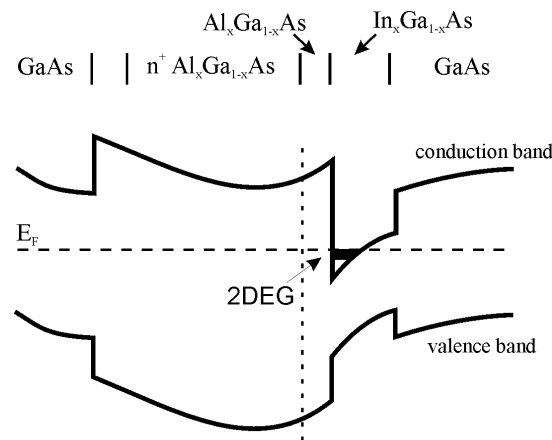


Fig. 35. The energy band profile of AlGaAs/InGaAs/GaAs PHEMT structure

A detailed study of a pseudomorphic Al_{0.22}Ga_{0.78}As/In_{0.21}Ga_{0.79}As/GaAs HEMT structure in the temperature range from liquid nitrogen to the room temperature was reported by Yin et al. [137]. The structure was fabricated with MBE on (001) GaAs substrate. It has similar profiles as those in HEMTs used for both low-noise and power amplification at 94 GHz. A 300 nm of not-intentionally doped GaAs, followed by 15 nm of In_{0.21}Ga_{0.79}As, 3 nm of Al_{0.22}Ga_{0.78}As, a planar Si doping layer of $5 \times 10^{12} \text{ cm}^{-2}$, 50 nm of Al_{0.22}Ga_{0.78}As and a 5 nm GaAs cap, was grown on the top of the buffer structure. From Hall measurements, sheet electron densities of $N_s = 2.3 \times 10^{12} \text{ cm}^{-2}$ at 77 K and $N_s = 2.5 \times 10^{12} \text{ cm}^{-2}$ at 300 K were determined.

Figure 36 shows both the PR and the electroreflectance (ER) spectra of PHEMT structure. The features below 1.4 eV, labelled A, B and C, are associated with InGaAs quantum well. The features between 1.4 eV and 1.45 eV originate from GaAs and those

at about 1.75 eV from the AlGaAs layer. The peaks at energies lower than those from AlGaAs, originate from GaAs/AlGaAs MQW. The part of the spectrum originating from InGaAs quantum well is the most interesting. Lineshapes of A, B and C features are unusual for modulation spectroscopy from a QW system. The traces should have positive and negative lobes but in this case they lie only on one side of the baseline. Also, the peak labelled as A is asymmetric on the high-energy side. This asymmetry property is due to the Fermi level filling factor. This enabled Yin et al. [137] to determine the Fermi energy and hence N_s .

In order to identify the origins of the A, B and C peaks, Yin et al. performed a self-consistent theoretical calculation. They found a very good agreement between ER experiment and theory associating features A, B and C with 21H, 32H and 42H transitions, respectively. Transitions which involve the ground electron subband are not allowed since E_F lies above this level. The densities of two-dimensional electron gas, obtained from the data, are in a good agreement with the Hall results. The Fermi energy (and hence N_s), obtained from the PR studies, is larger than that corresponding to the ER measurements. The discrepancy results from the presence of carriers photoexcited by the pump beam. Decreasing the pump light intensity can reduce the differences between the PR and ER spectra.

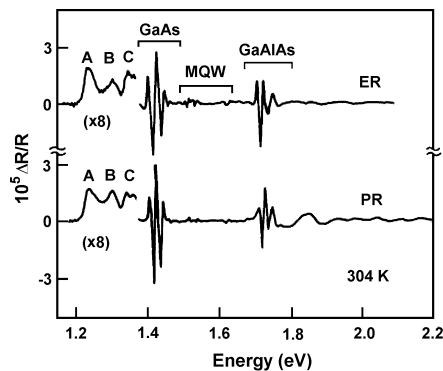


Fig. 36. Photoreflectance and electroreflectance spectra from AlGaAs/InGaAs/GaAs PHEMT structure. Features labelled A, B and C are associated with InGaAs quantum well (after Yin et al. [137])

Yin et al. [138] performed room-temperature PR investigations of three different AlGaAs/InGaAs/GaAs PHEMT structures. Besides the investigations of InGaAs region of the PR spectra, they studied features related to the GaAs and AlGaAs layers. They deduced electric fields corresponding to the GaAs and AlGaAs and also the Al composition. The field related to the GaAs signal is in agreement with the calculated built-in electric field. The Al composition also confirms the intended growth conditions.

Han et al. [139] studied the AlGaAs/InGaAs/AlGaAs PHEMT structures with different doping profiles. The doping on both sides of the InGaAs channel affects the electric field in GaAs and AlGaAs layers. The front side doping (Si delta-doped top AlGaAs layer, 2 nm from AlGaAs/InGaAs interface) influences mostly the Franz-Keldysh oscillations (electric field) in the AlGaAs layer, while back-side doping (Si-doped AlGaAs layer 3 nm below

InGaAs/AlGaAs interface) affects the Franz–Keldysh oscillations of the buffer GaAs feature. Han et al. [139] have not found any relationship between the electric field present in the structure and the channel carrier concentration.

There is a considerable interest in heterojunction bipolar transistor (HBT) technology for use in high-speed digital circuits and efficient microwave devices. The large valence band discontinuity at the emitter-base junction introduces an energy barrier which limits the injection of minority carriers from the base to the emitter. Hence, the emitter injection efficiency and the current gain can be improved significantly. An important drawback of HBT is a large collector–emitter offset voltage resulting from the turn-on voltage difference between the emitter–base heterojunction and base–collector homojunction.

Bottka et al. [140] studied AlGaAs/GaAs HBT structures grown by MOVPE technique. After growth, HBTs were fabricated in a portion of the wafer. In order to assess the transistor performance, current–voltage (I – V) and capacitance–voltage (C – V) characteristics were collected.

Figure 37 shows the PR spectra from the sample grown on a thick base layer (low current gain, $\beta = 5$), obtained using 400 Hz modulated 488 and 633 nm laser light. In part (a) of the figure, the damped oscillations between 1.45 and 1.7 eV correspond to the Franz–Keldysh oscillations mainly from the emitter-base space charge region. An electric field corresponding to these oscillations is about 130 kV/cm. In part (b) of the figure, an additional lower period Franz–Keldysh oscillation is observed in the spectral region between 1.44 and 1.5 eV. This feature originates from the base-collector space charge region. The oscillatory structure above 1.79 eV corresponds to the Franz–Keldysh oscillations of the $\text{Al}_x\text{Ga}_{1-x}\text{As}$ emitter layer, having an electric field of about 100 kV/cm. The $x = 0.28$ Al mole fraction was deduced from the energy gap.

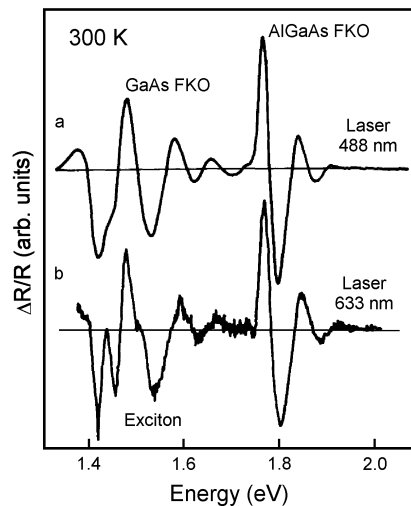


Fig. 37. Room-temperature photoreflectance spectra from a wide base AlGaAs/GaAs HBT structure (after Bottka et al. [140])

The base–emitter region is most critical for the overall device performance. A small difference in the placement of the base-emitter p-n junction can have considerable impact on the device. From the analysis of certain spectral features, Bottka et al. [140] evaluated the built-in DC electric field in both the AlGaAs emitter and in the n⁻ GaAs collector region.

Sun and Pollak [141] studied the origin of the Franz–Keldysh oscillations, observed in photoreflectance spectra, associated with the electric fields in the AlGaAs emitter and the GaAs collector of graded band gap heterojunction bipolar transistors. They derived analytical expressions for the origins of the Franz–Keldysh oscillations, associated with the fields in the graded emitter and collector regions of AlGaAs/GaAs HBT. The authors found that the oscillations from the collector are the measure of the maximum collector space charge field at the collector-base junction. The Franz–Keldysh oscillations, originating from the graded band gap AlGaAs emitter, are a function of both the space charge field and emitter-base grading dimension.

Compared to GaAs/AlGaAs based structures, lattice matched InP/In_{0.53}Ga_{0.47}As HBT structures have several advantages. Low turn-on voltage, low surface recombination rate and a use of the same substrates as sources and detectors of 1.3–1.55 μm wavelength radiation (favoured in optoelectronics) are some of the examples.

Using PR, Yan et al. [142] investigated a lattice-matched InP/In_{0.53}Ga_{0.47}As HBT structure grown by gas-source MBE. They performed a room-temperature measurement. From the periods of the Franz–Keldysh oscillations, they evaluated built-in electric fields to be 30 kV/cm and 100 kV/cm and corresponding donor levels of 4.5×10^{15} and 3.5×10^{16} cm⁻³ in n-InGaAs collector and n-InP emitter regions, respectively. The energy of the optical transition in InGaAs indicates that this material is lattice-matched to the InP.

A heterojunction bipolar transistor, based on InAlAs/InGaAs, has a break-down voltage lower than the two types of HBTs described above. Because of this fact, the InAlAs/InGaAs HBTs become an interesting topic in low-bias integrated-circuit applications. The simplest way to reduce the offset voltage is the method of inserting an intrinsic spacer, made of material with a small band gap, between the emitter and the base. Confining the two-dimensional electron gas, the spacer reduces the energy spike in the emitter-base junction.

Using photoreflectance spectroscopy, Chen et al. [143–146] studied lattice-matched InAlAs/InGaAs HBTs, grown by MBE. The structures were fabricated on an n⁺ InP:Si substrate (001). Two samples, with 30 nm and 50 nm width of the undoped InGaAs spacer layer, have been studied. Figure 38 shows a self-consistent calculated energy band diagram of a sample with the 30 nm spacer layer.

Photoreflectance spectra of the structures studied are presented in Fig. 39. Spectrum #1 comes from the structure with the 30 nm spacer and spectrum #2 is related to the structure with the 50 nm spacer. Features labelled as A and E denote the transitions due to the In_xGa_{1-x}As and the In_yAl_{1-y}As band gaps, respectively. From the energy position of these two features, In contents $x = 0.516$ and $y = 0.540$ were obtained. The quantum

confined excitonic transitions, with excitons formed by electrons confined to the QW in the emitter–spacer junction and unconfined holes in the valence band, are denoted as B. The features denoted as C are due to the electronic transitions between the valence band and a subband edge in the triangular quantum well in the spacer portion. The $E_0 + \Delta_0$ transitions in InGaAs are labelled D. The Franz–Keldysh oscillations near C and E are related to the built-in DC electric field. From the oscillations, Hsu et al. [143] found that the electric field in the InGaAs spacer and InAlAs emitter regions are 50.2 kV/cm and 107.6 kV/cm, respectively, for the sample with $L_S = 30$ nm and 41.4 kV/cm and 107.6 kV/cm for the sample with $L_S = 50$ nm. The electric field associated with C decreases as the spacer thickness increases. The authors estimated that the interface charge carrier density, N_S , is $3.54 \times 10^{11} \text{ cm}^{-2}$ for $L_S = 30$ nm and $4.22 \times 10^{11} \text{ cm}^{-2}$ for $L_S = 50$ nm.

Photoreflectance studies on the InAlAs/InGaAs HBT structure with $L_S = 30$ nm were continued by Chen and Jan [145]. They analyzed the behaviour of a two-dimensional electron gas at the temperatures between 10 K and 300 K. For the first time, Chen and Jan [145] utilized the temperature dependence of the effective mass to analyze Franz–Keldysh oscillations with the photoreflectance technique. The values deduced from the oscillations were in reasonable agreement with the calculations based on the intended growth condition.

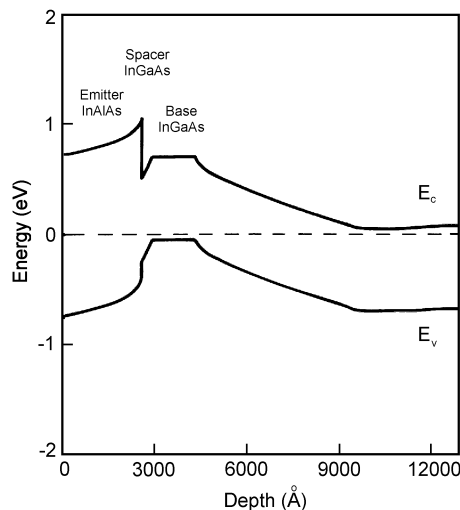


Fig. 38. Self-consistent calculated energy band diagram of InAlAs/InGaAs HBT with a spacer layer of 30 nm (after Chen et al. [144])

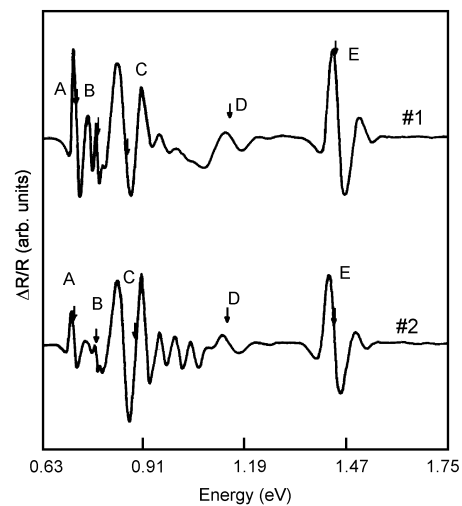


Fig. 39. The photoreflectance spectra from InAlAs/InGaAs HBTs with 30 nm (#1) and 50 nm (#2) spacer thickness. The origin of optical transitions marked with arrows is described in the text (after Hsu et al. [143])

Chen et al. [147] investigated graded InAlAs/InGaAs HBT structures at the temperatures between 8 K and 300 K. Using the Varshni and Bose–Einstein equations, they

described the temperature variation of energy gaps. From the observed Franz–Keldysh oscillations, they evaluated the built-in electric fields in the i-InGaAs collector, i-InGaAs spacer and n-InAlAs emitter regions. In the interfaces between the emitter and base, the electric field values agree with the continuity condition of electric displacements.

The n-p-n double-heterojunction bipolar transistor structure InGaP/InGaAsN/GaAs was characterized by Lin et al. [148] using polarized photoreflectance spectroscopy. The ordering parameter of the InGaP was deduced from the polarization ($[110]$ and $[1\bar{1}0]$) dependence of the PR signals from the emitter region. The ordering-related piezoelectric field was also found to influence the electric field, as evaluated from the Franz–Keldysh oscillations observed in the InGaP emitter region. The field in the emitter region was found to be about 25 kV/cm smaller than the theoretical value that does not take into account the possible ordering induced screening effect, while the field in the collector region agrees well with the theoretical value. In addition, the InGaAsN band gap was also determined by analyzing the PR spectrum of the base region.

6.2. Semiconductor lasers

The vertical cavity surface emitting laser (VCSEL) became recently very important in opto-electronics. VCSEL has several advantageous properties such as single longitudinal mode operation, small beam divergence, low threshold current and ease of integrability.

The photoreflectance results on VCSEL structures were reported by Berger et al. [149, 150]. The samples were grown by a gas source MBE. The structures consisted of an n^+ distributed Bragg reflector (DBR) as the bottom mirror, a cavity with three GaAs/AlGaAs QWs and a p^+ DBR as the top mirror. The full VCSEL structure described above is marked DU. The structure obtained at the same conditions but without top DBR is marked DT.

Berger et al. [149] recorded both the reflected signal RI_0 (not normalized reflectivity) and the modulated signal ΔRI_0 . A numerical division of ΔRI_0 by RI_0 gave the PR spectra. Reflected spectra and PR spectra obtained at room temperature for full structure (DU) and the structure without top DBR (DT) are plotted in Fig. 40. The dashed lines represent the RI_0 signal. For the DU structure, the RI_0 signal shows a reflectivity plateau of the cavity. Near 1.58 eV, RI_0 exhibits a slight dip, which is due to the resonance (Fabry–Perot) mode of the cavity. Solid lines represent PR spectra. The PR spectra in Fig. 40 exhibit two groups of features in each structure. A transition attributed to the quantum well occurs around 1.5 eV. Between 1.6 and 1.7 eV is a feature related to the AlGaAs layers. In the energy range of the plateau, both features in the DU spectrum are screened. Therefore, it is not possible to precisely determine the transition energies from this spectrum. The PR spectrum for the DT structure was used to determine the transition energies in the DU spectrum. Berger et al. [149] discovered that the features around 1.5 eV originate from the optical transition between the heavy hole and

the electron subbands. From the energy position of the AlGaAs related feature, the Al content of 16% was determined.

In order to change the quantum well transition energy, the measurements were performed at temperatures down to 9 K. The PR and R_{l_0} spectra for full VCSEL structure obtained at 300 K, 110 K and 9 K are shown in Fig. 41. In the PR spectra, the AlGaAs related transitions exhibit Franz–Keldysh oscillations, from which the value of the electric field in the cavity is estimated to be 38 kV/cm at a room temperature and decreases to 17 kV/cm at 9 K. At lower temperatures, the AlGaAs related transitions are no more screened. As the temperature decreases, the energy shift of QW transition is larger than the Fabry–Perot cavity mode shift. The intensity of the PR feature corresponding to the 11H transition rises as the temperature decreases. The maximum intensity was observed at 110 K. Two features around 1.57 eV are present in the spectrum recorded at 110 K. The higher energy feature originates from the 11H transition and the lower energy one corresponds to the Fabry–Perot cavity mode [150].

Klar et al. [151, 152] performed photoreflectance and conventional reflectance studies on an InGaAs/GaAs/AlGaAs vertical cavity surface emitting laser structure at a room temperature. The structure was grown by MBE on n^+ GaAs substrate. It was designed for operation at $\lambda = 1 \mu\text{m}$, and consists of a GaAs cavity with a 8.5 nm wide, compressively strained $\text{In}_{0.28}\text{Ga}_{0.72}\text{As}$ quantum well in the centre. The cavity is embedded between bottom (n^+) and top (p^+) distributed Bragg reflectors.

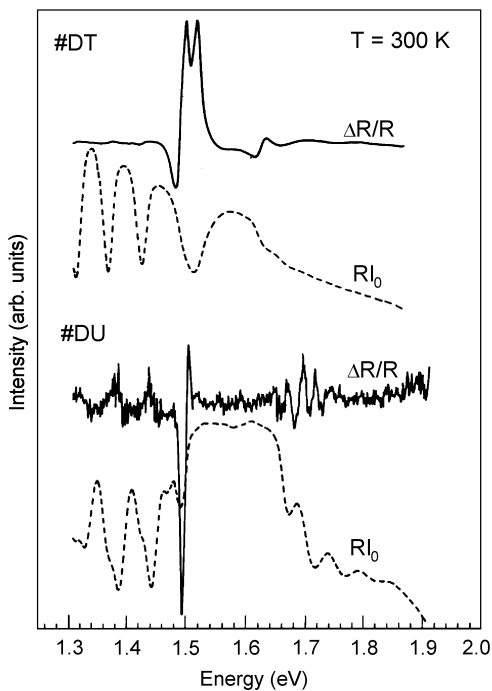


Fig. 40. Photoreflectance spectra at 300 K

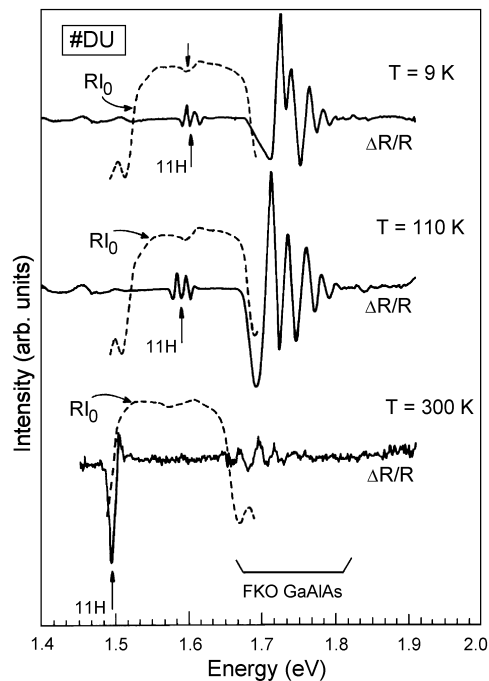


Fig. 41. Photoreflectance spectra from

<p>from the full VCSEL structure (#DU) and structure without a distributed Bragg reflector (#DT) – solid lines. Dashed lines represent reflected signal R/R_0 (after Berger et al. [149])</p>	<p>the full structure of a vertical cavity surface emitting laser (#DU) at 300 K, 110 K and 9 K (solid lines). Dashed lines hold for the reflected signal (after Berger et al. [149])</p>
------------------------------------------------------------------------------------------------------------------------------------------------------------------------------------------------------------	-------------------------------------------------------------------------------------------------------------------------------------------------------------------------------------------

Figure 42 shows a set of room-temperature PR spectra for different angles of incidence of the probe light. The spectra were taken with the lock-in amplifier set to detect $\Delta R/R$ signal, in-phase with respect to the constant PL background from the sample [151]. All the photoreflectance spectra show three prominent features. The first, at about 1.185 eV is 11H exciton transition in the $\text{In}_{0.28}\text{Ga}_{0.72}\text{As}$ quantum well. The second signal moves to a higher energy with increasing angle of incidence. It shows the same angular dependence as the cavity mode in the R spectrum, hence Klar et al. [151] conclude that this PR signal is due to the modulation of the cavity mode. Due to a variation in the In concentration, the ground-state QW transition is about 100 meV lower in energy than the cavity mode. The third signal, above 1.4 eV, is due to the FKO in the GaAs layers.

The strength of the signal from the cavity mode varies with the angle of incidence and is stronger between 30° and 60° than at the angles of 15° and 75° . This may be explained as follows. When the cavity mode feature overlaps in energy with a higher-order quantum well transition, probe light at this energy will be more strongly modulated by the QW than at other angles of incidence (such as 15° and 75°). Thus, one would expect a stronger photoreflectance signal for the cavity mode when it passes through positions of resonance with the higher-order QW transition, which are 12H, 13H, 21H and 22H for the QW being under study [151]. For the ranges of incidence between 30° and 60° , the cavity mode passes through 13H and 21H resonances.

The origin and lineshape of the photoreflectance signal associated with the cavity mode, Klar et al. [151] explained as follows. Due to the modulation-induced changes in the complex refractive index of the cavity layers, the cavity mode feature in the reflectance spectrum gives rise to a corresponding feature in the photoreflectance. Thus, the PR lineshape of this feature corresponds to the first derivative of the cavity mode dip in the reflectance spectrum.

Gosh et al. [153] report the PR studies on the coupling between the Fabry–Perot cavity mode (CM) and the QW ground-state excitonic feature in VCSEL structures. They applied changes in the symmetry of the CM-QW spectral feature by changing the angle of incidence of the probe beam.

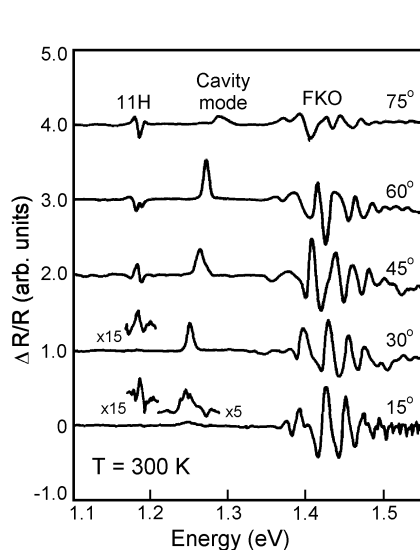


Fig. 42. Photoreflectance spectra from InGaAs/GaAs/AlGaAs VCSEL structure for different angles of incidence of the probe light (values indicated on the right) taken at a room temperature (after Klar et al. [151])

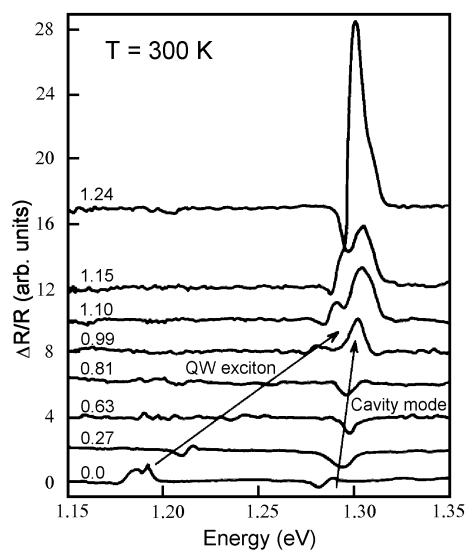


Fig. 43. Photoreflectance spectra from InGaAs/GaAs/AlGaAs VCSEL structure for various hydrostatic pressures. The pressure values in GPa are indicated on the left (after Klar et al. [152])

Klar et al. [152] continued the studies of InGaAs/GaAs/AlGaAs VCSEL structure, measuring the photoreflectance spectra at hydrostatic pressures up to 1.24 GPa. Figure 43 shows a series of photoreflectance spectra for various hydrostatic pressures. All the spectra display two signals. At ambient pressure, the low-energy signal at about 1.19 eV can be assigned to the 11H transition. The high-energy signal, at about 1.295 eV is attributed to the cavity mode. Both signals shift towards higher energy with increasing pressure. Because the energy shift of quantum well exciton feature is bigger than that of the cavity mode feature; at the highest pressure the overlap between those two features is observed.

From the photoreflectance data, Klar et al. [152] calculated the pressure coefficients for the QW exciton and the cavity mode, which are 92 meV/GPa and 15 meV/Gpa, respectively. The pressure coefficient for 11H transition is in agreement with the studies of strained InGaAs QWs embedded in GaAs barriers. The authors found that the value of the pressure coefficient for the cavity mode is mainly caused by the pressure-induced change of the refractive index of the cavity.

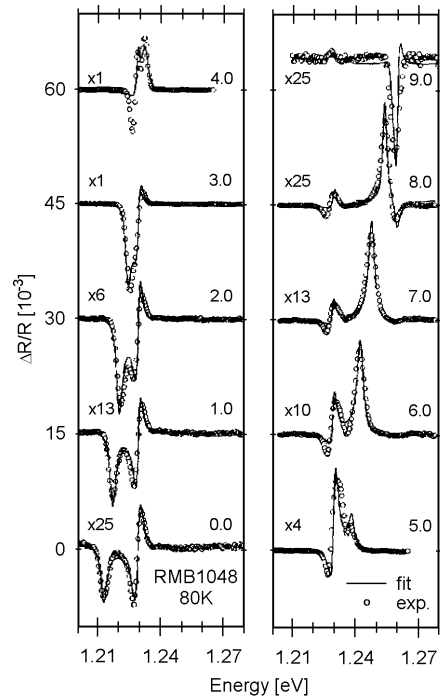


Fig. 44. Position-dependent PR spectra (open circles) of InGaAs/GaAs/AlAs at 80 K. By varying the position of the probe beam on the sample, indicated on the right (in mm), the cavity mode was tuned through resonance with the e1hh1 transition (after Klar et al. [154])

Because of the growth variations across the samples, there may be differences in the cavity mode energy, so that it can be tuned through the position of resonance with the QW ground-state exciton, by varying the position of measurement. Such investigations were performed by Klar et al. [154, 155] on the InGaAs/GaAs/AlAs microcavity VCSEL structures. Figure 44 depicts the PR spectra of VCSEL structure at 80 K in the spectral region near the cavity mode/e1hh1 exciton resonance, as a function of the probe beam position (in mm). The PR spectra clearly show two features which can be assigned to the cavity mode and the e1hh1 exciton. The e1hh1 transition energy does not depend noticeably on the probe position but the cavity feature increases in energy with increasing micrometer setting, crossing the energy of the e1hh1 exciton. The resonance occurs near the 4.0 mm position. From the scaling factor indicated on the left of Fig. 44 it may be seen that the PR signal strength is enhanced at resonance by the factor of 25. Although the PR signals of e1hh1 exciton and cavity mode are clearly distinguishable when they do not overlap, a complicated lineshape arises when they do.

The InGaAs/GaAs/GaAlAs VCSEL structure was investigated using photoreflectance, normal-incidence reflectivity (NIR) and surface photovoltage spectroscopy (SPS) in the temperature range between 15 K and 400 K by Huang et al. [156]. The PR data show only the ground (1C–1H) excitonic transition (and FKOs) while the cavity mode is detected by NIR. The changes of the energy of the ground state and the cavity mode

energy with temperature are shown in Fig. 45. The open circles and squares in Fig. 45 are $E_{1C-1H}(T)$ and $E_{cav}(T)$, respectively, from the SPS investigation.

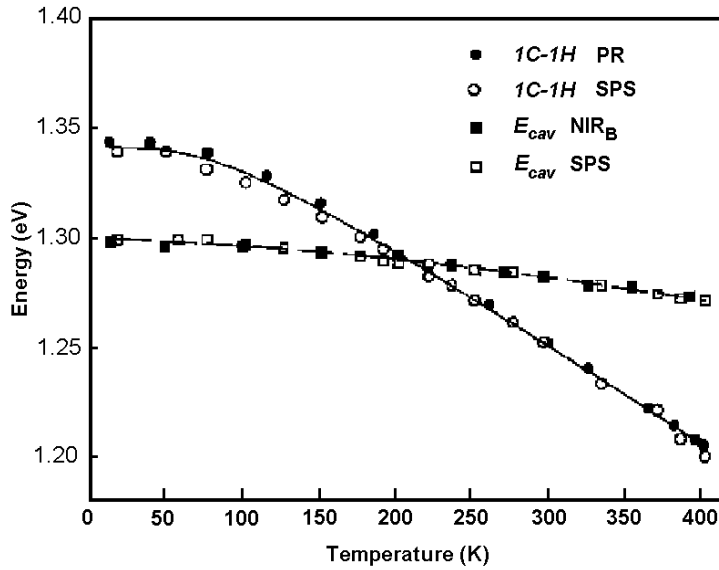


Fig. 45. The changes of the energy of the ground state and the cavity mode energy with temperature. The open circles and squares are $E_{1C-1H}(T)$ and $E_{cav}(T)$, respectively, as determined from the SPS. The solid circles and squares are $E_{1C-1H}(T)$ and $E_{cav}(T)$ as determined from PR and NIR, respectively. The solid and dashed lines are least-square fits to a Bose–Einstein-like expression and a quadratic term, respectively (after Huang et al. [156])

The closed circles and squares in Fig. 45 are $E_{1C-1H}(T)$ and $E_{cav}(T)$, respectively, as determined from the PR and NIR spectra. There is a good agreement between the SPS data and the relevant PR/NIR measurements. The solid line in Fig. 45 is a least-squares fit of $E_{1C-1H}(T)$ to a Bose–Einstein-type expression. The quantity $E_{cav}(T)$ has been fit to a quadratic expression. Basing on the above-mentioned structural characteristics for the relevant portions of the sample, the calculated field in the i-GaAs region is 60 kV/cm, what is substantially higher than the field determined from the FKOs.

Pollak et al. [157] investigated multiple quantum well planar emitting laser structures. They performed a room-temperature PR study of two pseudomorphic InGaAsP/InP 1.3 μm MQW laser structures. The structures were fabricated by the MOCVD technique. The first structure was grown on a (001) InP substrate with a n^+ InP buffer. A lattice-matched InGaAsP separate confinement heterostructures (SCH) about 50 nm thick, followed by 6–10 InGaAsP QWs (strained layers) with lattice-matched InGaAsP barriers were grown on the buffer layer. The MQW stack was followed by another lattice-matched InGaAsP SCH and by a p^+ InP layer. The entire structure was covered with a lattice-matched InGaAsP cap.

Figure 46 presents the room-temperature PR spectrum of a structure with 6 nm QWs. The features below 1.1 eV originate from the MQW stack. The signal above 1.3 eV comes from the top InP p^+ layer. The feature exhibits the Franz–Keldysh oscillations which can be used to find information about the built-in electric field in this region. Between these two groups of features is a Franz–Keldysh oscillation originating from the SCH. The built-in electric field in the SCH region is about 41 kV/cm. The band gap of SCH material is 1.104 eV, which means that the materials are lattice-matched.

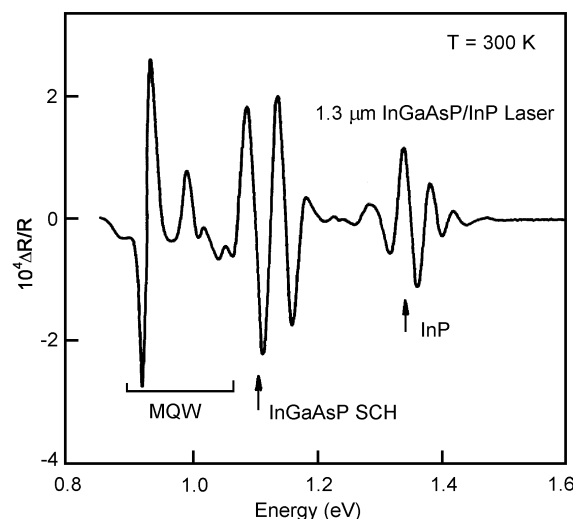


Fig. 46. Photoreflectance spectrum from a pseudomorphic 1.3 μm InGaAsP/InP MQW laser structure with QWs 6 nm wide (after Pollak et al. [157])

A lineshape fit made it possible to accurately determine the energies of five quantum transitions in the MQW. The lowest energy feature is due to the 11H optical transition. This transition is responsible for the lasing frequency of the structure. The energy of 11H transition is 0.925 eV (1.34 μm).

Aigouy et al. [158] evaluated the energy of the fundamental transition (11H) in a 0.98 μm InGaAs/GaAs/InGaP p-i-n quantum well laser, as a function of both the bias applied to the laser, and the position on the laser stripe. They used photoreflectance as well electroreflectance techniques with a spatial resolution of about 10 μm . The laser device was grown by MOCVD on an n^+ GaAs (001) substrate. The active region consisted of two undoped pseudomorphic 7-nm $\text{In}_{0.19}\text{Ga}_{0.81}\text{As}$ QWs separated by a 20-nm undoped GaAs barrier. The active region was surrounded on each side by 85 nm of GaAs, sandwiched between n- and p-type InGaP.

The application of a forward bias results in a blue shift in the 11H transition energy, a decrease in the linewidth and an increase in the amplitude of the spectral feature. Re-

verse bias has the opposite effect. These changes in various parameters are a consequence of the quantum confined Stark effect. At zero bias, the QWs are in the electric field of the p-i-n structure. Application of the bias changes the electric field, giving rise to a shift of the transition energy and to changes of other parameters. Aigouy et al. [158] evaluated the electric field to be 70 kV/cm at zero bias.

They also performed a scan of the 11H transition energy vs. the localization of the probe light spot on the surface of laser structure. They scanned a surface of 750×50 μm and found spatial variations in the 11H transition energy of 6–7 meV over the entire region, which are probably due to inhomogeneities in composition and the electric field distribution.

Dilute-N InGaAs/GaAs based laser structure designed to emit at 1.3 μm was investigated by Choulis et al. [159]. Interdiffusion effects performed by dielectric capping and rapid thermal annealing of the InGaAsP-based laser structures were studied by Kudrawiec et al. [160].

7. Summary

In this article, we presented the review of the experimental, theoretical and instrumentation aspects of photorefectance spectroscopy. The photorelectance is extremely useful since it is contactless and does not require any special mounting of the sample. Moreover, photorelectance can be carried out even at room temperature, providing as much information as other optical methods (PL, PLE) at very low temperatures. It can be utilized under a wide variety of conditions such as elevated temperatures (e.g. in situ monitoring of growth), stress, external electric field or magnetic field.

The emphasis of this paper has been placed on the investigation of the properties of semiconductor bulk, low-dimensional semiconductor structures and semiconductor device structures, mainly in relation to the electronic band structure and its consequences. Refined theories, particularly the low-field first and third derivative formulations and the Franz–Keldysh model of electromodulation, enabled investigators to quantitatively analyze the photorelectance spectra. The sharp, derivative like features of photomodulated signals made it possible to conveniently investigate the band structure of a wide variety of semiconductors and to explore the influence of different perturbations like temperature, strain, built-in electric field, growth and processing.

Acknowledgements

This work was partly supported by the Centre for Advanced Materials and Nanotechnology, Wrocław University of Technology.

Abbreviations

2DEG	–two-dimensional electron gas
CB	–conduction band

DBR	–distributed Bragg reflector
DQW	–double quantum well
ER	–electroreflectance
FDGL	–first-derivative Gaussian lineshape
FDLL	–first-derivative Lorentzian lineshape
FFT	–fast Fourier transformation
FKO	–Franz–Keldysh oscillations
HBT	–heterojunction bipolar transistor
HEMT	–high electron mobility transistor
HH or hh	–heavy holes
LH or lh	–light holes
MBE	–molecular beam epitaxy
ML	–monolayer
MOCVD	–metal-organic chemical vapour deposition
MOVPE	–metal-organic vapour-phase epitaxy
MQW	–multiple quantum well
NIR	–normal-incidence reflectivity
PHEMT	–pseudomorphic high electron mobility transistor
PL	–photoluminescence
PLE	–photoluminescence excitation
PR	–photoreflectance
PRD	–photoreflectance-difference
PT	–phototransmittance
QD	–quantum dot
QW	–quantum well
R	–reflectivity
RIE	–reactive ion etching
RTA	–rapid thermal annealing
SCH	–separate confinement heterostructures
SL	–superlattice
SPS	–surface photovoltage spectroscopy
TDFE	–third-derivative functional form
TEM	–transmission electron microscopy
VB	–valence band
VCSEL	–vertical cavity surface emitting laser

References

- [1] GLEMBOCKI O.J., SHANBROOK B.V., BOTTKA N., BEARD W.T., COMAS J., *Appl. Phys. Lett.*, 46 (1985), 970.
- [2] GLEMBOCKI O.J., SHANABROOK B.V., *Photoreflectance spectroscopy of microstructures*, [in:] D.G. Seiler, C.L. Littler. (Eds.), *Semiconductors and Semimetals*, Vol. 36, Academic Press, New York, 1992, p. 221.
- [3] POLLAK F.H., GLEMBOCKI O.J., *Proc. SPIE*, 946 (1988), 2.
- [4] POLLAK F.H., QIANG H., YAN D., YIN Y., BOCCIO V.T., *Photonics Spectra*, 27 (1993), 78.
- [5] POLLAK F.H., *Modulation spectroscopy of semiconductors and semiconductor microstructures*, [in:] M. Balkanski (Ed.), *Handbook on Semiconductors*, Vol. 2, Elsevier, Amsterdam, 1994, p. 527.
- [6] GLEMBOCKI O.J., *Proc. SPIE*, 1286 (1990), 2.
- [7] MISIEWICZ J., SĘK G., SITAREK P., *Optica Applicata*, 29 (1999), 327.

- [8] MISIEWICZ J., SITAREK P., SĘK G., *Opto-electr. Rev.*, 8 (2000), 1.
- [9] PHILLIP H.R., EHRENREICH H., *Phys. Rev.*, 129 (1963), 1550.
- [10] ASPNES D.E., STUDNA A.A., *Phys. Rev. B* 7 (1973), 4605.
- [11] KLAR P.J., TOWNSLEY C.M., WOLVERSON D., DAVIES J.J., ASHENFORD D.E., LUNN B., *Semicond. Sci. Technol.*, 10 (1995), 1568.
- [12] SERAPHIN B.O., BOTTKA N., *Phys. Rev.*, 145 (1966), 628.
- [13] ASPNES D.E., *Surface Sci.*, 37 (1973), 418.
- [14] ASPNES D.E., *Phys. Rev.*, 153 (1967), 972.
- [15] ASPNES D.E., *Handbook on Semiconductors*, Vol. 2, [in:] M. Balkanski (Ed.), North Holland, Amsterdam, 1980, p. 109.
- [16] SHANABROOK B.V., GLEBOCKI O.J., BEARD W.T., *Phys. Rev. B* 35 (1987), 2540.
- [17] HUANG Y.S., QIANG H., POLLAK F.H., LEE J., ELMAN B., *J. Appl. Phys.*, 70 (1991), 3808.
- [18] ASPNES D.E., *Phys. Rev. B* 10 (1974), 4228.
- [19] SHEN H., POLLAK F.H., *Phys. Rev. B* 42 (1990), 7097.
- [20] THEIS W., SANDERS M., LEAK G.D., BAJAJ C.E., MORKOÇ H., *Phys. Rev. B* 37 (1988), 3042.
- [21] GLEBOCKI O.J., SHANABROOK B.V., *Proc. SPIE*, 794 (1987), 12.
- [22] MARKIEWICZ P., Report of the Institute of Physics WUT, SPR 287, (1995), in Polish.
- [23] SHEN H., DUTTA M., *Appl. Phys. Lett.*, 57 (1990), 587.
- [24] SYDOR M., BADAKHSHAN A., *J. Appl. Phys.*, 70 (1991), 2322.
- [25] MISIEWICZ J., ZHENG X.L., BECLA P., HEIMAN D., *Solid State Commun.*, 66 (1988), 351.
- [26] ISHITANI Y., HAMADA H., MINAGAWA S., YAGUCHI H., SHIRAKI Y., *Jpn. J. Appl. Phys.*, 36 (1997), 6607.
- [27] SHIRAKATA S., CHICHIBU S., ISOMURA S., *Jpn. J. Appl. Phys.*, 36 (1997), 7160.
- [28] SHIRAKATA S., CHICHIBU S., ISOMURA S., *Jpn. J. Appl. Phys.*, 36 (1997), 6645.
- [29] CHICHIBU S. F., TSUKAZAKI A., KAWASAKI M., TAMURA K., SEGAWA Y., SOTA T., KOINUMA H., *Appl. Phys. Lett.*, 80 (2002), 2860.
- [30] SHAN W., LITTLE B.D., SONG J.J., FENG Z.C., SHURMAN M., STALL R.A., *Appl. Phys. Lett.*, 69 (1996), 3315.
- [31] SITAREK P., MISIEWICZ J., VEJE E., *Proc. SPIE*, 3725 (1999), 205.
- [32] SITAREK P., MISIEWICZ J., VEJE E., *Adv. Mater. Opt. Electr.*, 10 (1999), 261.
- [33] EL ALLALI M., SORENSEN C.B., VEJE E., TIDEMAND-PETERSSON P., *Phys. Rev. B* 48 (1993), 4398.
- [34] PETERS L., PHANEUF L., KAPITAN L.W., THEIS W.M., *J. Appl. Phys.*, 62 (1987), 4558.
- [35] LEE C., LEE N.Y., KIM J.E., PARK H.Y., KWAK D.H., LEE H.C., LIM H., *J. Appl. Phys.*, 77 (1995), 6727.
- [36] JEZERSKI K., SITAREK P., MISIEWICZ J., PANEK M., ŚCIANA B., KORBUTOWICZ R., TŁACZAŁA M., *Vacuum*, 48 (1997), 277.
- [37] ZHANG X., CHUA S.J., LIU W., CHONG K.B., *Appl. Phys. Lett.*, 72 (1998), 1890.
- [38] BADAKHSHAN A., GLOSSER R., LAMBERT S., *J. Appl. Phys.*, 69 (1991), 2525.
- [39] VARSHNI K.P., *Physica*, 34 (1967), 149.
- [40] LAUTENSCHLAGER P., CARRIGA M., CARDONA M., *Phys. Rev. B* 35 (1987), 9174.
- [41] LAUTENSCHLAGER P., CARRIGA M., CARDONA M., *Phys. Rev. B* 36 (1987), 4813.
- [42] SHEN H., HANG Z., PAN S.H., POLLAK F.H., WOODALL J.M., *Appl. Phys. Lett.*, 52 (1988), 2058.
- [43] RÖPPISCHER H., STEIN N., BEHN U., NOVIKOV A.B., *J. Appl. Phys.*, 76 (1994), 4340.
- [44] HANG Z., SHEN H., POLLAK F.H., *Solid State Commun.*, 73 (1990), 15.
- [45] POLLAK F.H., *Proc. SPIE*, 1361 (1991), 109.
- [46] HANG Z., YAN D., POLLAK F.H., PETTIT G.D., WOODALL J.M., *Phys. Rev. B* 44 (1991), 10546.
- [47] CHEN J.H., CHI W.S., HUANG Y.S., YIN Y., POLLAK F.H., PETTIT G.D., WOODALL J.M., *Semicon. Sci. Technol.*, 8 (1993), 1420.
- [48] CHI W.S., HUANG Y.S., QIANG H., POLLAK F.H., PETTIT D.G., WOODALL J.M., *Jpn. J. Appl. Phys.*, 33 (1994), 966.

- [49] KUAN H., SU Y.K., WU T.S., HUANG Y.S., CHI W.S., *Sol. State Electron.*, 39 (1996), 885.
- [50] BOUAMAMA K., HÖRIG W., NEUMANN H., *Semicond. Sci. Technol.*, 13 (1998), 75.
- [51] BELLANI V., AMIOTTI M., GEDDO M., GUIZZETTI G., LANDGREN G., *Mat. Res. Soc. Symp. Proc.*, 324 (1994), 225.
- [52] GEDDO M., BELLANI V., GUIZZETTI G., *Phys. Rev. B* 50 (1994), 5456.
- [53] MUNOZ M., POLLAK F.H., ZAKIA M.B., PATEL N. B., HERRERA-PEREZ J. L., *Phys. Rev. B* 62 (2000), 16600.
- [54] PAL U., HERRERA PEREZ J.L., PIQUERAS J., DIEGUEZ E., *Mater. Sci. Eng. B* 42 (1996), 297.
- [55] SHEN S.C., ZHANG L.J., LU W., BICKNELL-TASSIUS R.N., *Sol. State Electron.*, 37 (1994), 1087.
- [56] LIN C.H., SINGER K.E., EVANS-FREEMAN J.H., HEATH K., MISSOUS M., *Semicond. Sci. Technol.*, 12 (1997), 1619.
- [57] LI C.F., HUANG Y.S., MALIKOVA L., POLLAK F.H., *Phys. Rev. B* 55 (1997), 9251.
- [58] GLEMOCKI O.J., *Mater. Res. Soc. Symp. Proc.*, 160 (1990), 631.
- [59] SĘK G., TALIK S., MISIEWICZ J., RADZIEWICZ D., TŁACZAŁA M., PANEK M., KORBUTOWICZ R., *Electron Technol.*, 30 (1997), 366.
- [60] SĘK G., MISIEWICZ J., RADZIEWICZ D., TŁACZAŁA M., PANEK M., KORBUTOWICZ R., *Vacuum*, 50 (1998), 219.
- [61] FITZGERALD E.A., *Properties of Lattice-Matched and Strained Indium Gallium Arsenide*, [in:] P. Bhattacharaya (Ed.), IEE EMIS Datareviews Series 8, 1993, p. 6.
- [62] LASTRAS-MARTINEZ L.F., CHAVIRA-RODRIGUEZ M., LASTRAS-MARTINEZ A., BALDERAS-NAVARRO R.E., *Phys. Rev. B* 66 (2002), 075315.
- [63] LASTRAS-MARTINEZ A., BALDERAS-NAVARRO R.E., LASTRAS-MARTINEZ L.F., VIDAL M.A., *Phys. Rev. B* 59 (1999), 10234.
- [64] ANDREANI L.C., DE NOVA D., DI LERNIA S., GEDDO M., GUIZZETTI G., PATRINI M., BOCCHI C., BOSACCHI A., FERRARI C., FRENCHI S., *J. Appl. Phys.*, 78 (1995), 6745.
- [65] RADHAKRISHNAN K., YOON S.F., LI H.M., HAN Z.Y., ZHANG D.H., *J. Appl. Phys.*, 76 (1994), 246.
- [66] MO S., PEINER E., BARTELS A., TANG G.P., SCHLACHETZKI A., KUZMENKO R., HILDEBRANDT S., SCHREIBER J., *Jpn. J. Appl. Phys.*, 35 (1996), 4238.
- [67] LEE J.H., JANG K.S., SHIN C.S., PARK H.L., KIM T.W., *J. Appl. Phys.*, 75 (1994), 8216.
- [68] HAN M.S., KANG T.W., KIM T.W., *Solid. State Commun.*, 105 (1998), 709.
- [69] CHICHIBU S., SHIKANAI A., AZUHATA T., SOTA T., KURAMATA A., HORINO K., NAKAMURA S., *Appl. Phys. Lett.*, 68 (1996), 3766.
- [70] TCHOUNKEU M., BRIOT O., GIL B., ALEXIS J.P., AULOMBARD R.L., *J. Appl. Phys.*, 80 (1996), 5352.
- [71] SHIKANAI A., AZUHATA T., SOTA T., CHICHIBU S., KURAMATA A., HORINO K., NAKAMURA S., *J. Appl. Phys.*, 81 (1997), 417.
- [72] ALEMU A., GIL B., JULIER M., NAKAMURA S., *Phys. Rev. B* 57 (1998), 3761.
- [73] SITAREK P., KUDRAWIEC R., SĘK G., MISIEWICZ J., PASZKIEWICZ R., KORBUTOWICZ R., PASZKIEWICZ B., TŁACZAŁA M., *Mat. Sci. Eng. B* 82 (2001), 209.
- [74] KUDRAWIEC R., SĘK G., MISIEWICZ J., PASZKIEWICZ R., PASZKIEWICZ B., TŁACZAŁA M., *Mat. Sci. Eng. B* 96 (2002), 284.
- [75] WANG D.P., SHEN T.L., *Jpn. J. Appl. Phys.*, 33 (1993), 1253.
- [76] JEZIEFSKI K., MISIEWICZ J., MARKIEWICZ P., PANEK M., ŚCIANA B., TŁACZAŁA M., KORBUTOWICZ R., *Phys. Stat. Sol. (a)*, 147 (1995), 467.
- [77] JEZIEFSKI K., SITAREK P., MISIEWICZ J., PANEK M., ŚCIANA B., KORBUTOWICZ R., TŁACZAŁA M., *Vacuum*, 48 (1997), 277.
- [78] WANG Z., PAN S., HUANG S., ZHANG C., MU S., ZHOU X., JIAN J., XU G., CHEN Z., *J. Phys. D: Appl. Phys.*, 26 (1993), 1493.
- [79] WANG Z., PAN S., MU S., *Phys. Stat. Sol. (a)*, 140 (1993), 135.
- [80] JEZIEFSKI K., SITAREK P., MISIEWICZ J., PANEK M., ŚCIANA B., KORBUTOWICZ R., TŁACZAŁA M., *Acta Phys. Pol.*, 88 (1995), 751.
- [81] YOSHITA M., TAKAHASHI T., *Appl. Surf. Sci.*, 115 (1997), 347.

- [82] SCHEIBLER H.E., ALPEROVICH V.L., JAROSHEVICH A.S., TEREKHOV A.S., Phys. Stat. Sol. (a), 152 (1995), 113.
- [83] WANG D. P., CHEN C. T., Appl. Phys. Lett., 67 (1995), 2069.
- [84] WANG D.P., CHEN C.C., SHEN T.L., HSU T.M., LEE W.C., J. Appl. Phys., 80 (1996), 6980.
- [85] NUKEAW J., MATSUBARA N., FUJIWARA Y., TAKEDA Y., Appl. Surf. Sci., 117/118 (1997), 776.
- [86] NUKEAW J., FUJIWARA Y., TAKEDA Y., Jpn. J. Appl. Phys., 36 (1997), 7019.
- [87] CHANG W.H., HSU T.M., LEE W.C., CHUANG R.S., J. Appl. Phys., 83 (1998), 7873.
- [88] NOWACZYK M., SĘK G., MISIEWICZ J., ŚCIANA B., RADZIEWICZ D., TŁACZAŁA M., Thin Solid Films, 380 (2000), 243.
- [89] YIN X., CHEN H.M., POLLAK F.H., CHAN Y., MONTANO P.A., KIRCHNER P.D., PETTIT G.D., WOODALL J.M., J. Vac. Sci. Technol., A10 (1992), 131.
- [90] OH Y.T., BYUN S.C., LEE B.R., KANG T.W., HONG C.Y., PARK S.B., LEE H.K., KIM T.W., J. Appl. Phys., 76 (1994), 1959.
- [91] YAN D., POLLAK F.H., CHIN T.P., WOODALL J.M., Phys. Rev. B52 (1995), 4674.
- [92] NAKANISHI H., WADA K., WALUKIEWICZ W., J. Appl. Phys., 78 (1995), 5103.
- [93] MOCHIZUKI Y., ISHII T., MIZUTA M., MOCHIZUKI A., LANGER J. M., Phys. Rev. Lett., 77 (1996), 3601.
- [94] LOPEZ-LOPEZ M., MELENDEZ-LIRA M., GOTO S., Appl. Phys. Lett., 71 (1997), 338.
- [95] LEE W.C., HSU T.M., WANG S.C., CHANG M.N., CHYI J.I., J. Appl. Phys., 83 (1998), 486.
- [96] BADAKHSHAN A., ENGLAND J.L., THOMPSON P., CHEUNG P., YANG C.H., ALAVI K., J. Appl. Phys., 81 (1997), 910.
- [97] GLEBOCKI O.J., TUCHMAN J.A., DAGATA J.A., KO K.K., PANG S.W., STUTZ C.E., Appl. Phys. Lett., 73 (1998), 114.
- [98] PAGET D., KIERREN B., HOUDRÉ R., J. Vac. Sci. Technol. A16 (1998), 2350.
- [99] KLAR P.J., GRÜNING H., GÜNGERICH M., HEIMBRODT W., KOCH J., TORUNSKI T., STOLZ W., POLIMENI A., CAPIZZI M., Phys. Rev. B67 (2003), 121206(R).
- [100] KUDRAWIEC R., SĘK G., MISIEWICZ J., LI L.H., HARMAND J.C., Appl. Phys. Lett., 83 (2003), 1379.
- [101] CARDONA M., *Modulation Spectroscopy*, Academic Press, New York, 1969.
- [102] SITAREK P., SĘK G., MISIEWICZ J., CHENG T.S., Vacuum, 50 (1998), 203.
- [103] SITAREK P., SĘK G., MISIEWICZ J., CHENG T.S., Inst.Phys.Conf. Ser., 152 (1998), 657.
- [104] BASTARD G., *Wave Mechanics Applied to Semiconductor Heterostructures*, Les Editions de Physique, Paris, 1992.
- [105] ZUCKER J.E., PINCZUK A., CHEMLA D.S., GOSSARD A.C., WIEGMANN W., Phys. Rev. B29 (1984), 7065.
- [106] SONG J.J., YOON Y.S., FEDOROWSKY A., KIM Y.B., SCHULMAN J.N., TU C.W., HUANG D.M., MORKOÇ H., Phys. Rev. B 34 (1986), 8958.
- [107] REDDY U.K., JI G., HENDERSON T., MORKOÇ H., SCHULMAN J.N., J. Appl. Phys., 62 (1987), 145.
- [108] JI G., DOBBELAERE W., HUANG D., MORKOÇ H., Phys. Rev. B39 (1989), 3216.
- [109] SHEN H., PAN S.H., HANG Z., POLLAK F.H., SACKS R.N., Solid State Commun., 65 (1988), 929.
- [110] TSENG S. M., CHEN Y. F., CHENG Y. T., HSU C. W., HUANG Y. S., LIN D. Y., Phys. Rev. B64 (2001), 195311.
- [111] PAN S.H., SHEN H., HANG Z., POLLAK F.H., ZHUANG W., XU Q., ROTH A.P., MASUT R.A., LACELLE C., MORRIS D., Phys. Rev. B38 (1988), 3375.
- [112] SĘK G., MISIEWICZ J., RADZIEWICZ D., TŁACZAŁA M., PANEK M., KOR BUTOWICZ R., Vacuum, 50 (1998), 199.
- [113] KUDRAWIEC R., SĘK G., RUDNO-RUDZIŃSKI W., MISIEWICZ J., WÓJCIK J., ROBINSON B.J., THOMPSON D.A., MASCHER P., Acta Phys. Pol. A102 (2002), 649.
- [114] SITAREK P., RYCZKO K., SĘK G., MISIEWICZ J., FISCHER M., REINHARDT M., FORCHEL A., Solid State Electr., 47 (2003), 489.
- [115] MISIEWICZ J., SITAREK P., RYCZKO K., KUDRAWIEC R., FISCHER M., REINHARDT M., FORCHEL A., Microelectronics J., 34 (2003), 737.

- [116] HEROUX J. B., YANG X., WANG W. I., *J. Appl. Phys.*, 92 (2002), 4361.
- [117] KUDRAWIEC R., SĘK G., MISIEWICZ J., GOLLUB D., FORCHEL A., *Appl. Phys. Lett.*, (2003), in press.
- [118] KUDRAWIEC R., SĘK G., RYCZKO K., MISIEWICZ J., SUNDGREN P., ASPLUND C., HAMMAR M., *Solid State Commun.*, 127 (2003), 613.
- [119] CHOULIS S.A., HOSEA T.J.C., TOMIĆ S., KAMAL-SAAFI M., ADAMS A.R., O'REILLY E.P., WEINSTEIN B.A., KLAR P.J., *Phys. Rev. B* 66 (2002), 165321-1.
- [120] KUDRAWIEC R., SĘK G., RYCZKO K., MISIEWICZ J., FORCHEL A., *Superlattices and Microstructures*, 32 (2002), 19.
- [121] WETZEL C., TAKEUCHI T., AMANO H., AKASAKI I., *Phys. Rev. B* 61 (2000), 2159.
- [122] WETZEL C., TAKEUCHI T., AMANO H., AKASAKI I., *Phys. Rev. B* 62 (2000), R13302.
- [123] SĘK G., RYCZKO K., KUBISA M., MISIEWICZ J., KOETH J., FORCHEL A., *Opto-Electr. Rev.*, 7 (1999), 117.
- [124] SĘK G., RYCZKO K., MISIEWICZ J., BAYER M., WANG T., FORCHEL A., *Acta Phys. Pol. A* 100 (2001), 417.
- [125] CHO Y.-H., KIM D.-S., JHE W., *Appl. Phys. Lett.*, 78 (2001), 2306.
- [126] QIANG H., POLLAK F.H., TANG Y.S., WANG P.D., SOTOMAYOR TORRES C.M., *Appl. Phys. Lett.*, 64 (1994), 2830.
- [127] GUMBS G., HUANG D., QIANG H., POLLAK F.H., WANG P.D., SOTOMAYOR TORRES C.M., HOLLAND M.C., *Phys. Rev. B* 50 (1994), 10962.
- [128] WANG D.P., SOTOMAYOR TORRES C.M., HOLLAND M.C., QIANG H., POLLAK F.H., GUMBS G., *Mat. Res. Soc. Symp. Proc.*, 324 (1994), 187.
- [129] KLAR P.J., WOLVERSON D., ASHENFORD D.E., LUNN B., HENNING T., *Semicond. Sci. Technol.*, 11 (1996), 1863.
- [130] ULRICH C., VES S., GONI A.R., KURTENBACH A., SYASSEN K., EBERL K., *Phys. Rev. B* 52 (1995), 12212.
- [131] SĘK G., MISIEWICZ J., RYCZKO K., KUBISA M., HEINRICHS DORFF F., STIER O., BIMBERG D., *Solid State Commun.*, 110 (1999), 657.
- [132] SĘK G., RYCZKO K., MISIEWICZ J., BAYER M., KLOPF F., REITHMAIER J. P., FORCHEL A., *Solid State Commun.*, 117 (2001), 401.
- [133] MISIEWICZ J., SĘK G., KUDRAWIEC R., *Current Appl. Phys.*, (2003), in press.
- [134] SOARES J.A.N.T., BELIAEV D., ENDERLEIN R., SCOLFARO L.M.R., SAITO M., LEITE J.R., *Mat. Sci. Eng.*, B35 (1995), 267.
- [135] ENDERLEIN R., *Phys. Stat. Sol. (b)*, 194 (1996), 257.
- [136] SĘK G., MISIEWICZ J., CHENG T.S., *Adv. Mater. Opt. Electron.*, 7 (1997), 241.
- [137] YIN Y., QIANG H., POLLAK F.H., STREIT D.C., WOJCIWICZ M., *Appl. Phys. Lett.*, 61 (1992), 1579.
- [138] YIN Y., QIANG H., YAN D., POLLAK F.H., NOBLE T.F., *Semicond. Sci. Technol.*, 8 (1993), 1599.
- [139] HAN A.C., WOJCIWICZ M., PASCUA D., BLOCK T.R., STREIT D.C., *J. Appl. Phys.*, 82 (1997), 2607.
- [140] BOTTKA N., GASKILL D.K., WRIGHT P.D., KALISKI R.W., WILLIAMS D.A., *J. Cryst. Growth*, 107 (1991), 893.
- [141] SUN W.D., POLLAK F.H., *J. Appl. Phys.*, 83 (1998), 4447.
- [142] YAN D., POLLAK F.H., BOCCIO V.T., LIN C.L., KIRCHNER P.D., WOODALL J.M., GEE R.C., ASBECK P.M., *Appl. Phys. Lett.*, 61 (1992), 2066.
- [143] HSU K.T., CHEN Y.H., CHEN K.L., LIN H.H., JAN G.J., *Appl. Phys. Lett.*, 64 (1994), 1974.
- [144] CHEN Y.H., HSU K.T., CHEN K.L., LIN H.H., JAN G.J., *Jpn. J. Appl. Phys.*, 33 (1994), 2448.
- [145] CHEN Y.H., JAN G.J., *J. Appl. Phys.*, 77 (1995), 6681.
- [146] CHEN Y.H., JAN G.J., *IEEE J. Quantum Electron.*, 33 (1997), 574.
- [147] CHEN K.L., LIN H.H., JAN G.J., CHEN Y.H., Tseng P.K., *J. Appl. Phys.*, 78 (1995), 4035.
- [148] LIN C. J., HUANG Y. S., LI N. Y., LI P. W., TIONG K. K., *J. Appl. Phys.*, 90 (2001) 4565.
- [149] BERGER P.D., BRU C., BENYATOU T., CHENEVAS-PAULE A., GROSSE P., *Proc. SPIE*, 2397 (1995), 726.
- [150] BERGER P.D., BRU C., BENYATOU T., GUILLOT G., CHENEVAS-PAULE A., COUTURIER L., GROSSE P., *Appl. Phys. Lett.*, 68 (1996), 4.
- [151] KLAR P.J., ROWLAND G., SALE T.E., HOSEA T.J.C., GREY R., *Phys. Stat. Sol. (a)*, 170 (1998), 145.

- [152] KLAR P.J., VINCENTE P.M.A., SALE T.E., HOSEA T.J.C., ADAMS A.R., RAYMOND A., *Solid State Commun.*, 107 (1998), 97.
- [153] GHOSH S., HOSEA T.J.C., CONSTANT S.B., *Appl. Phys. Lett.*, 78 (2001), 3250.
- [154] KLAR P.J., ROWLAND G., THOMAS P.J.S., ONISCHENKO A., SALE T.E., HOSEA T.J.C., GREY R., *Phys. Rev. B* 59 (1999), 2894.
- [155] KLAR P.J., ROWLAND G., THOMAS P.J.S., ONISCHENKO A., SALE T.E., HOSEA T.J.C., GREY R., *Phys. Rev. B* 59 (1999,) 2902.
- [156] HUANG Y. S., MALIKOVA L., POLLAK F.H., SHEN H., PAMULAPATI J., NEWMAN P., *Appl. Phys. Lett.*, 77 (2000), 37.
- [157] POLLAK F.H., KRYSZEK W., LEIBOVITCH M., MALIKOVA L., HYBERTSEN M.S., LUM R., VANDENBERG J.M., REYNOLDS C.L., *Proc. SPIE*, 2693 (1996), 455.
- [158] AIGOUY L., POLLAK F.H., GUMBS G., *Appl. Phys. Lett.*, 70 (1997), 2562.
- [159] CHOULIS S.A., TOMI S., O'REILLY E.P., HOSEA T.J.C., *Solid State Commun.*, 125 (2003), 155.
- [160] KUDRAWIEC R., SĘK G., RYCZKO K., RUDNO-RUDZIŃSKI W., MISIEWICZ J., WÓJCIK J., ROBINSON B.J., THOMPSON D.A., MASCHER P., *Physica E* 17 (2003), 602.

Figures were reproduced by the permission of: American Institute of Physics (Figs. 6, 7, 28, 36, 39, 45), American Physical Society (Figs. 8, 9, 14, 20, 21, 29, 44), Elsevier Science B.V. (Figs. 1, 33, 37, 43), International Society for Optical Engineering (SPIE) (Figs. 22, 40, 41, 46), Japanese Journal of Applied Physics (Fig. 38), Wiley-VCH Verlag GmbH & Co. KGaA (Fig. 42), Materials Research Society (Fig. 10).

Received 23 April 2003

Revised 19 May 2003